

Article

An Elastic Interface Model for the Delamination of Bending-Extension Coupled Laminates

Stefano Bennati , Paolo Fisicaro , Luca Taglialegne  and Paolo S. Valvo * 

Department of Civil and Industrial Engineering, University of Pisa, Largo Lucio Lazzarino, I-56122 Pisa, Italy

* Correspondence: p.valvo@ing.unipi.it; Tel.: +39-050-2218223

Received: 23 July 2019; Accepted: 24 August 2019; Published: 30 August 2019



Abstract: The paper addresses the problem of an interfacial crack in a multi-directional laminated beam with possible bending-extension coupling. A crack-tip element is considered as an assemblage of two sublaminates connected by an elastic-brittle interface of negligible thickness. Each sublaminate is modeled as an extensible, flexible, and shear-deformable laminated beam. The mathematical problem is reduced to a set of two differential equations in the interfacial stresses. Explicit expressions are derived for the internal forces, strain measures, and generalized displacements in the sublaminates. Then, the energy release rate and its Mode I and Mode II contributions are evaluated. As an example, the model is applied to the analysis of the double cantilever beam test with both symmetric and asymmetric laminated specimens.

Keywords: fiber-reinforced composite laminate; multi-directional laminate; delamination; elastic interface; energy release rate; mixed-mode fracture

1. Introduction

Delamination, or interlaminar fracture, is the main life-limiting failure mode for fiber-reinforced composite laminates [1]. Delamination cracks may originate from localized defects and propagate due to peak interlaminar stresses. A huge number of analytical, numerical, and experimental studies have been devoted to this problem during the last few decades [2–6]. The phenomenon is also relevant for many similar layered structures, such as glued laminated timber beams [7] and multilayered ceramic composites [8].

Within the framework of linear elastic fracture mechanics (LEFM), a delamination crack is expected to propagate when the energy release rate, \mathcal{G} , attains a critical value, or fracture toughness, \mathcal{G}_c . Since delamination cracks preferentially propagate along the weak interfaces between adjoining plies (laminae), propagation generally involves a mix of the three basic fracture modes (Mode I or opening, Mode II or sliding, and Mode III or tearing). Each fracture mode furnishes an additive contribution to the total energy release rate, \mathcal{G}_I , \mathcal{G}_{II} , and \mathcal{G}_{III} [9], and corresponds to a different value of interlaminar fracture toughness, \mathcal{G}_{Ic} , \mathcal{G}_{IIc} , and \mathcal{G}_{IIIc} [10]. Thus, to predict delamination crack propagation, it is necessary (i) to assess by experiments the interlaminar fracture toughness (in pure and mixed fracture modes), (ii) to define a suitable mixed-mode fracture criterion, and (iii) to use a theoretical model to evaluate the energy release rate and its modal contributions [11].

An effective modeling approach to evaluate the energy release rate is to consider a delaminated laminate as composed of sublaminates connected by an elastic interface, i.e., a continuous distribution of linearly elastic–brittle springs. Such an elastic interface model was developed first by Kanninen for the double cantilever beam (DCB) test specimen [12] and later adopted by many authors for the analysis of the delamination of composite laminates [13–26]. Elastic interface models can be regarded as particular cases of the more general cohesive-zone models [27,28]. The latter are increasingly used to model delamination associated with large-scale bridging and other non-linear damage

phenomena [29–38]. A parallel line of research concerns adhesively-bonded joints, for which models of growing complexity have been proposed in the literature [39]: from elastic interface models [40–46] to non-linear cohesive-zone models [47,48].

Bending-extension coupling and other elastic couplings are a typical feature of composite laminated beams and plates [49]. Nevertheless, only a few theoretical models for the study of delamination take into account elastic couplings. Among these, it is worth citing the pioneering work by Schapery and Davidson on the prediction of the energy release rate in mixed-mode fracture conditions [50]. In recent years, Xie et al. considered bending-extension coupling in the analysis of delamination toughness specimens [36] and composite laminated plates subjected to flexural loading [25]. Dimitri et al. presented a general formulation of the elastic interface model including bending-extension and shear deformability, but limited their analytical solution to the case with no elastic coupling [26]. Valvo analyzed the delamination of shear-deformable laminated beams with bending-extension coupling based on a rigid interface model [51]. Tsokanas and Loutas extended the above-mentioned analysis to include the effects of crack tip rotations and hygrothermal stresses [52]. To the best of our knowledge, a complete analytical solution for the elastic interface model of delaminated beams with bending-extension coupling and shear deformability has not yet been presented in the literature.

This paper analyses the problem of an interfacial crack in a multi-directional laminated beam with possible bending-extension coupling [53]. A crack-tip element is defined as a laminate segment extending ahead and behind the crack tip cross-section, such that the fracture process zone is fully included within [54,55]. In line with the elastic interface modeling approach, the crack-tip element is considered as an assemblage of two sublaminates connected by an elastic-brittle interface of negligible thickness. Each sublaminate is modeled as an extensible, flexible, and shear-deformable laminated beam [56]. The mathematical problem is reduced to a set of two differential equations in the interfacial stresses. A complete analytical solution is derived including explicit expressions for the internal forces, strain measures, and generalized displacements in the sublaminates. Then, the energy release rate and its Mode I and Mode II contributions are evaluated based on Rice's \mathcal{J} -integral [57]. By way of illustration, the model is applied to the analysis of the DCB test. Three laminated specimens are analyzed, made up of uni-directional, cross-ply, and multi-directional sublaminates.

2. Crack-Tip Element

2.1. Mechanical Model

Let us consider a composite laminated beam of length L , width B , and thickness $H = 2h$, with a through-the-width delamination crack of length a . The delamination plane ideally subdivides the laminate into two sublaminates (labeled 1 and 2) of thicknesses $H_1 = 2h_1$ and $H_2 = 2h_2$. We fix a right-handed global Cartesian reference system, $Oxyz$, with the origin O at the center of the crack tip cross-section and the x -, y -, and z -axes aligned with the laminate longitudinal, width, and thickness directions, respectively (Figure 1).

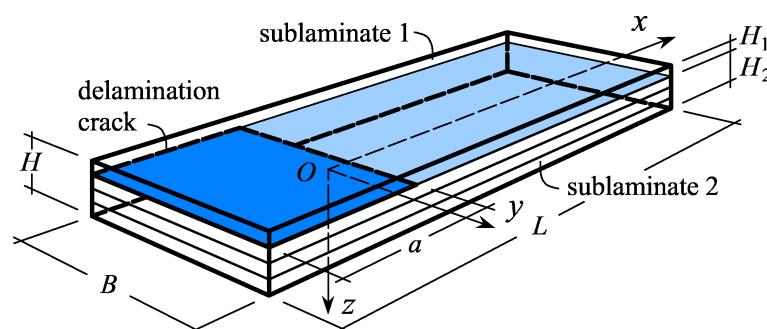


Figure 1. Laminated beam with through-the-width delamination.

The present mechanical model focuses on a *crack-tip element (CTE)*, here defined as a laminate segment of length ℓ , extending ahead and behind the crack tip cross-section, which fully includes the fracture process zone [54,55]. In practice, the end sections of the CTE, A and B , should be chosen such that A is immediately ahead of the delamination front and B is sufficiently far from it to make sure that the laminate behind behaves as a monolithic beam (Figure 2a). We model the sublaminates as two plane beams connected by an elastic-brittle interface of negligible thickness. The *generalized displacements* for the sublaminates are defined as follows: u_α and w_α denote the sublaminate mid-plane displacements along the x - and z -directions, respectively; φ_α denote their cross-section rotations about the y -axis (positive if counter-clockwise). Henceforth, the subscript α is used to refer to the upper ($\alpha = 1$) and lower ($\alpha = 2$) sublaminates (Figure 2b).

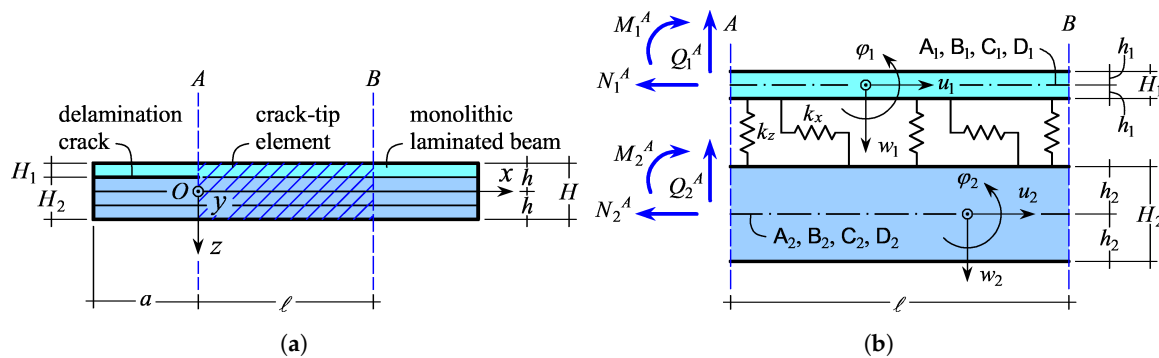


Figure 2. Crack-tip element: (a) definition; (b) model.

In line with the kinematics of Timoshenko’s beam theory [56], we define the *strain measures* for the sublaminates as the *mid-plane axial strain*, ϵ_α , *average shear strain*, γ_α , and *pseudo-curvature*, κ_α . These are related to the generalized displacements as follows:

$$\epsilon_\alpha = \frac{du_\alpha}{dx}, \quad \gamma_\alpha = \frac{dw_\alpha}{dx} + \varphi_\alpha, \quad \text{and} \quad \kappa_\alpha = \frac{d\varphi_\alpha}{dx}. \tag{1}$$

Next, we introduce the conjugated *internal forces*, namely the *axial force*, N_α , *shear force*, Q_α , and *bending moment*, M_α . For a laminated beam with bending-extension coupling, the internal forces are related to the strain measures as follows:

$$N_\alpha = A_\alpha \epsilon_\alpha + B_\alpha \kappa_\alpha, \quad Q_\alpha = C_\alpha \gamma_\alpha, \quad \text{and} \quad M_\alpha = B_\alpha \epsilon_\alpha + D_\alpha \kappa_\alpha, \tag{2}$$

where A_α , B_α , C_α , and D_α respectively denote the sublaminate *extensional stiffness*, *bending-extension coupling stiffness*, *shear stiffness*, and *bending stiffness*. In general, such stiffnesses should be calculated according to classical laminated plate theory [49], as detailed in Appendix A.

For what follows, it is convenient to introduce also the sublaminate compliances,

$$a_\alpha = \frac{D_\alpha}{A_\alpha D_\alpha - B_\alpha^2}, \quad b_\alpha = -\frac{B_\alpha}{A_\alpha D_\alpha - B_\alpha^2}, \quad c_\alpha = \frac{1}{C_\alpha}, \quad \text{and} \quad d_\alpha = \frac{A_\alpha}{A_\alpha D_\alpha - B_\alpha^2}, \tag{3}$$

and write the constitutive relations, Equation (2), in inverse form:

$$\epsilon_\alpha = a_\alpha N_\alpha + b_\alpha M_\alpha, \quad \gamma_\alpha = c_\alpha Q_\alpha, \quad \text{and} \quad \kappa_\alpha = b_\alpha N_\alpha + d_\alpha M_\alpha. \tag{4}$$

The elastic interface between the upper and lower sublaminates transfers both normal and shear *interfacial stresses*, respectively given by:

$$\sigma = k_z \Delta w \quad \text{and} \quad \tau = k_x \Delta u, \tag{5}$$

where k_z and k_x are the *interface elastic constants* and:

$$\Delta w = w_2 - w_1 \quad \text{and} \quad \Delta u = u_2 - u_1 - \varphi_2 h_2 - \varphi_1 h_1 \tag{6}$$

are the transverse and longitudinal *relative displacements* at the interface, respectively. By substituting Equation (6) into (5), we obtain:

$$\sigma = k_z (w_2 - w_1) \quad \text{and} \quad \tau = k_x (u_2 - u_1 - \varphi_2 h_2 - \varphi_1 h_1). \tag{7}$$

2.2. Differential Problem

The equilibrium equations for the upper and lower sublaminates are:

$$\frac{dN_\alpha}{dx} + n_\alpha = 0, \quad \frac{dQ_\alpha}{dx} + q_\alpha = 0, \quad \text{and} \quad \frac{dM_\alpha}{dx} + m_\alpha - Q_\alpha = 0, \tag{8}$$

where n_α , q_α , and m_α respectively are the *distributed axial load*, *transverse load*, and *bending couple*, due to the normal and shear stresses transferred by the interface:

$$n_1 = -n_2 = B\tau, \quad q_1 = -q_2 = B\sigma, \quad \text{and} \quad m_\alpha = B\tau h_\alpha. \tag{9}$$

We substitute Equation (9) into (8) and differentiate the latter with respect to x . Then, by using Equations (1)–(4), we obtain the set of governing differential equations for the upper sublaminate,

$$\begin{aligned} \frac{1}{B} \frac{d^3 u_1}{dx^3} &= -(a_1 + b_1 h_1) \frac{d\tau}{dx} - b_1 \sigma, \\ \frac{1}{B} \frac{d^4 w_1}{dx^4} &= (b_1 + d_1 h_1) \frac{d\tau}{dx} - c_1 \frac{d^2 \sigma}{dx^2} + d_1 \sigma, \quad \text{and} \\ \frac{1}{B} \frac{d^3 \varphi_1}{dx^3} &= -(b_1 + d_1 h_1) \frac{d\tau}{dx} - d_1 \sigma, \end{aligned} \tag{10}$$

and for the lower sublaminate,

$$\begin{aligned} \frac{1}{B} \frac{d^3 u_2}{dx^3} &= (a_2 - b_2 h_2) \frac{d\tau}{dx} + b_2 \sigma, \\ \frac{1}{B} \frac{d^4 w_2}{dx^4} &= -(b_2 - d_2 h_2) \frac{d\tau}{dx} + c_2 \frac{d^2 \sigma}{dx^2} - d_2 \sigma, \quad \text{and} \\ \frac{1}{B} \frac{d^3 \varphi_2}{dx^3} &= (b_2 - d_2 h_2) \frac{d\tau}{dx} + d_2 \sigma. \end{aligned} \tag{11}$$

2.3. Boundary Conditions

The crack-tip element is subjected to known internal forces on the upper and lower sublaminates at cross-section A . Hence, the following six static boundary conditions can be written:

$$\begin{aligned} N_1|_{x=0} &= N_1^A, & Q_1|_{x=0} &= Q_1^A, & M_1|_{x=0} &= M_1^A; \\ N_2|_{x=0} &= N_2^A, & Q_2|_{x=0} &= Q_2^A, & M_2|_{x=0} &= M_2^A. \end{aligned} \tag{12}$$

At cross-section B , three kinematic boundary conditions can be obtained from the assumption that the laminate behind behaves as a monolithic beam:

$$\begin{aligned} \epsilon_1|_{x=\ell} + \kappa_1|_{x=\ell} h_1 &= \epsilon_2|_{x=\ell} - \kappa_2|_{x=\ell} h_2, \\ \gamma_1|_{x=\ell} &= \gamma_2|_{x=\ell}, \quad \text{and} \quad \kappa_1|_{x=\ell} &= \kappa_2|_{x=\ell}. \end{aligned} \tag{13}$$

To sum up, we have nine boundary conditions to complete the formulation of the differential problem. We note that, in general, no restraints are given to prevent rigid-body motions of the CTE.

3. Solution of the Differential Problem

3.1. Solution Strategy

Following a solution strategy already adopted to solve some specific problems [22,43,44,53], the interfacial stresses are here assumed as the main unknowns. To this aim, we differentiate the normal and shear interfacial stresses, Equation (7), four and three times, respectively, with respect to x . Then, we substitute Equations (10) and (11) into the result. After some simplifications, we obtain the following differential equation set:

$$\begin{aligned} \frac{d^4\sigma}{dx^4} - \alpha_1 \frac{d^2\sigma}{dx^2} + \alpha_2\sigma + k_z\beta_0 \frac{d\tau}{dx} &= 0, \\ \frac{d^3\tau}{dx^3} - \alpha_3 \frac{d\tau}{dx} - k_x\beta_0\sigma &= 0, \end{aligned} \tag{14}$$

where:

$$\begin{aligned} \alpha_1 &= k_zB(c_1 + c_2), \quad \alpha_2 = k_zB(d_1 + d_2), \quad \text{and} \\ \alpha_3 &= k_xB(a_1 + a_2 + 2b_1h_1 - 2b_2h_2 + d_1h_1^2 + d_2h_2^2) \end{aligned} \tag{15}$$

are constant coefficients and:

$$\beta_0 = B(b_1 + b_2 + d_1h_1 - d_2h_2) \tag{16}$$

is a coupling parameter, here called the *unbalance parameter* by analogy with the literature on adhesive joints [39].

Two cases have to be considered in solving the differential problem:

(1) the *balanced case*, when $\beta_0 = 0$, i.e., $d_1h_1 + b_1 = d_2h_2 - b_2$. This condition is trivially fulfilled, for instance, by homogeneous laminates with mid-plane delaminations (for which $b_1 = b_2 = 0$, $d_1 = d_2$, and $h_1 = h_2$) or symmetrically-stacked laminates with mid-plane delaminations (for which $b_1 = -b_2$, $d_1 = d_2$, and $h_1 = h_2$). Besides, the balance condition is satisfied by homogeneous sublaminates with bending stiffness ratio $\frac{D_1}{D_2} = \frac{h_1}{h_2}$ [38,58]. More generally, it is possible to conceive of non-trivial stacking sequences, where the upper and lower sublaminates have unequal thicknesses, but fulfil the balance condition [59,60]. In the balanced case, Equations (14) are uncoupled and can be solved separately to obtain the normal and shear interfacial stresses;

(2) the *unbalanced case*, when $\beta_0 \neq 0$, i.e., $d_1h_1 + b_1 \neq d_2h_2 - b_2$. This condition corresponds to laminates with generic stacking sequences and arbitrarily-located delaminations (with respect to the mid-plane). In the unbalanced case, Equations (14) are coupled and must be solved simultaneously.

In the following subsections, we will show how to solve the stated differential problem and obtain the expressions for the interfacial stresses. Then, by using Equations (1), (4) and (8), it is straightforward to deduce also the expressions for the internal forces, strain measures, and generalized displacements.

3.2. Balanced Case

3.2.1. Interfacial Stresses

In the balanced case, the differential problem, Equation (14), reduces to the following two uncoupled differential equations:

$$\begin{aligned} \frac{d^4\sigma}{dx^4} - \alpha_1 \frac{d^2\sigma}{dx^2} + \alpha_2\sigma &= 0, \\ \frac{d^3\tau}{dx^3} - \alpha_3 \frac{d\tau}{dx} &= 0, \end{aligned} \tag{17}$$

whose coefficients are defined in Equation (15).

The general solution for the interfacial stresses in the balanced case can be written as follows:

$$\begin{aligned} \sigma(x) &= \frac{1}{B} \sum_{i=1}^4 f_i \exp(-\lambda_i x), \\ \tau(x) &= \frac{1}{B} [f_5 \exp(-\lambda_5 x) + f_6 \exp(-\lambda_6 x) + f_7], \end{aligned} \tag{18}$$

where f_1, f_2, \dots, f_7 are integration constants and:

$$\begin{aligned} \lambda_1 &= \frac{1}{\sqrt{2}} \sqrt{\alpha_1 - \sqrt{\alpha_1^2 - 4\alpha_2}}, \quad \lambda_2 = -\lambda_1, \\ \lambda_3 &= \frac{1}{\sqrt{2}} \sqrt{\alpha_1 + \sqrt{\alpha_1^2 - 4\alpha_2}}, \quad \lambda_4 = -\lambda_3, \\ \lambda_5 &= \sqrt{\alpha_3}, \quad \text{and} \quad \lambda_6 = -\lambda_5 \end{aligned} \tag{19}$$

are the non-zero roots of the characteristic equation of the differential problem (17):

$$(\lambda^4 - \alpha_1\lambda^2 + \alpha_2)(\lambda^2 - \alpha_3) = 0. \tag{20}$$

Strictly speaking, the solution expressed by Equation (18) holds provided that the interface constant k_z is not equal to the following “critical” value:

$$\hat{k}_z = \frac{4}{B} \frac{d_1 + d_2}{(c_1 + c_2)^2}, \tag{21}$$

for which Equation (20) has coincident roots and the solution requires a different expression. However, for material properties corresponding to common fiber-reinforced laminates, the numerical values of k_z are usually greater than \hat{k}_z , and the roots of the characteristic equation are real-valued (see Appendix B.1). For very compliant interfaces, e.g., if the present model is applied to the analysis of adhesively-bonded joints with weak adhesive, it may happen that $k_z < \hat{k}_z$, and the characteristic equation has complex roots. In such cases, the present solution is still valid, provided that the complex exponential functions are considered in Equation (18) and the following. Similar considerations apply also to the unbalanced case.

3.2.2. Internal Forces

By substituting Equation (18) into (9), the latter into (8), and integrating with respect to x , we obtain the expressions for the internal forces in the upper sublaminates,

$$\begin{aligned} N_1(x) &= \frac{f_5}{\lambda_5} \exp(-\lambda_5 x) + \frac{f_6}{\lambda_6} \exp(-\lambda_6 x) - f_7 x - f_8, \\ Q_1(x) &= \sum_{i=1}^4 \frac{f_i}{\lambda_i} \exp(-\lambda_i x) - f_{10}, \quad \text{and} \\ M_1(x) &= - \sum_{i=1}^4 \frac{f_i}{\lambda_i^2} \exp(-\lambda_i x) + \frac{h_1 f_5}{\lambda_5} \exp(-\lambda_5 x) + \frac{h_1 f_6}{\lambda_6} \exp(-\lambda_6 x) - (f_{10} + h_1 f_7) x - f_{12}, \end{aligned} \tag{22}$$

and in the lower sublamine,

$$N_2(x) = -\frac{f_5}{\lambda_5} \exp(-\lambda_5 x) - \frac{f_6}{\lambda_6} \exp(-\lambda_6 x) + f_7 x + f_9,$$

$$Q_2(x) = -\sum_{i=1}^4 \frac{f_i}{\lambda_i} \exp(-\lambda_i x) + f_{11}, \quad \text{and} \tag{23}$$

$$M_2(x) = \sum_{i=1}^4 \frac{f_i}{\lambda_i^2} \exp(-\lambda_i x) + \frac{h_2 f_5}{\lambda_5} \exp(-\lambda_5 x) + \frac{h_2 f_6}{\lambda_6} \exp(-\lambda_6 x) + (f_{11} - h_2 f_7) x + f_{13},$$

where f_8, f_9, \dots, f_{13} are integration constants.

3.2.3. Strain Measures

By substituting Equations (22) and (23) into (4), we obtain the expressions for the strain measures in the upper sublamine,

$$\begin{aligned} \epsilon_1(x) &= (a_1 + b_1 h_1) \left[\frac{f_5}{\lambda_5} \exp(-\lambda_5 x) + \frac{f_6}{\lambda_6} \exp(-\lambda_6 x) \right] - b_1 \sum_{i=1}^4 \frac{f_i}{\lambda_i^2} \exp(-\lambda_i x) + \\ &\quad - [(a_1 + b_1 h_1) f_7 + b_1 f_{10}] x - a_1 f_8 - b_1 f_{12}, \\ \gamma_1(x) &= c_1 \sum_{i=1}^4 \frac{f_i}{\lambda_i} \exp(-\lambda_i x) - c_1 f_{10}, \quad \text{and} \tag{24} \\ \kappa_1(x) &= -d_1 \sum_{i=1}^4 \frac{f_i}{\lambda_i^2} \exp(-\lambda_i x) + (d_1 h_1 + b_1) \left[\frac{f_5}{\lambda_5} \exp(-\lambda_5 x) + \frac{f_6}{\lambda_6} \exp(-\lambda_6 x) \right] + \\ &\quad - [(d_1 h_1 + b_1) f_7 + d_1 f_{10}] x - b_1 f_8 - d_1 f_{12}, \end{aligned}$$

and in the lower sublamine,

$$\begin{aligned} \epsilon_2(x) &= - (a_2 - b_2 h_2) \left[\frac{f_5}{\lambda_5} \exp(-\lambda_5 x) + \frac{f_6}{\lambda_6} \exp(-\lambda_6 x) \right] + b_2 \sum_{i=1}^4 \frac{f_i}{\lambda_i^2} \exp(-\lambda_i x) + \\ &\quad + [(a_2 - b_2 h_2) f_7 + b_2 f_{11}] x + a_2 f_9 + b_2 f_{13}, \\ \gamma_2(x) &= -c_2 \sum_{i=1}^4 \frac{f_i}{\lambda_i} \exp(-\lambda_i x) + c_2 f_{11}, \quad \text{and} \tag{25} \\ \kappa_2(x) &= d_2 \sum_{i=1}^4 \frac{f_i}{\lambda_i^2} \exp(-\lambda_i x) + (d_2 h_2 - b_2) \left[\frac{f_5}{\lambda_5} \exp(-\lambda_5 x) + \frac{f_6}{\lambda_6} \exp(-\lambda_6 x) \right] + \\ &\quad - [(d_2 h_2 - b_2) f_7 - d_2 f_{11}] x + b_2 f_9 + d_2 f_{13}. \end{aligned}$$

3.2.4. Generalized Displacements

Lastly, by substituting Equations (24) and (25) into (1) and integrating the latter with respect to x , we obtain the expressions for the generalized displacements in the upper sublamine,

$$\begin{aligned}
 u_1(x) &= - (a_1 + b_1 h_1) \left[\frac{f_5}{\lambda_5^2} \exp(-\lambda_5 x) + \frac{f_6}{\lambda_6^2} \exp(-\lambda_6 x) \right] + b_1 \sum_{i=1}^4 \frac{f_i}{\lambda_i^3} \exp(-\lambda_i x) + \\
 &\quad - [(a_1 + b_1 h_1) f_7 + b_1 f_{10}] \frac{x^2}{2} - (a_1 f_8 + b_1 f_{12}) x + f_{14}, \\
 w_1(x) &= \sum_{i=1}^4 \left(\frac{d_1}{\lambda_i^2} - c_1 \right) \frac{f_i}{\lambda_i^2} \exp(-\lambda_i x) - (d_1 h_1 + b_1) \left[\frac{f_5}{\lambda_5^3} \exp(-\lambda_5 x) + \frac{f_6}{\lambda_6^3} \exp(-\lambda_6 x) \right] + \\
 &\quad + [(d_1 h_1 + b_1) f_7 + d_1 f_{10}] \frac{x^3}{6} + (b_1 f_8 + d_1 f_{12}) \frac{x^2}{2} - (f_{16} + c_1 f_{10}) x + f_{15}, \quad \text{and} \\
 \varphi_1(x) &= d_1 \sum_{i=1}^4 \frac{f_i}{\lambda_i^3} \exp(-\lambda_i x) - (d_1 h_1 + b_1) \left[\frac{f_5}{\lambda_5^2} \exp(-\lambda_5 x) + \frac{f_6}{\lambda_6^2} \exp(-\lambda_6 x) \right] + \\
 &\quad - [(d_1 h_1 + b_1) f_7 + d_1 f_{10}] \frac{x^2}{2} - (b_1 f_8 + d_1 f_{12}) x + f_{16},
 \end{aligned} \tag{26}$$

and in the lower sublimate,

$$\begin{aligned}
 u_2(x) &= (a_2 - b_2 h_2) \left[\frac{f_5}{\lambda_5^2} \exp(-\lambda_5 x) + \frac{f_6}{\lambda_6^2} \exp(-\lambda_6 x) \right] - b_2 \sum_{i=1}^4 \frac{f_i}{\lambda_i^3} \exp(-\lambda_i x) + \\
 &\quad + [(a_2 - b_2 h_2) f_7 + b_2 f_{11}] \frac{x^2}{2} + (a_2 f_9 + b_2 f_{13}) x + f_{17}, \\
 w_2(x) &= - \sum_{i=1}^4 \left(\frac{d_2}{\lambda_i^2} - c_2 \right) \frac{f_i}{\lambda_i^2} \exp(-\lambda_i x) - (d_2 h_2 - b_2) \left[\frac{f_5}{\lambda_5^3} \exp(-\lambda_5 x) + \frac{f_6}{\lambda_6^3} \exp(-\lambda_6 x) \right] + \\
 &\quad + [(d_2 h_2 - b_2) f_7 - d_2 f_{11}] \frac{x^3}{6} - (b_2 f_9 + d_2 f_{13}) \frac{x^2}{2} - (f_{19} - c_2 f_{11}) x + f_{18}, \quad \text{and} \\
 \varphi_2(x) &= - d_2 \sum_{i=1}^4 \frac{f_i}{\lambda_i^3} \exp(-\lambda_i x) - (d_2 h_2 - b_2) \left[\frac{f_5}{\lambda_5^2} \exp(-\lambda_5 x) + \frac{f_6}{\lambda_6^2} \exp(-\lambda_6 x) \right] + \\
 &\quad - [(d_2 h_2 - b_2) f_7 - d_2 f_{11}] \frac{x^2}{2} + (b_2 f_9 + d_2 f_{13}) x + f_{19},
 \end{aligned} \tag{27}$$

where $f_{14}, f_{15}, \dots, f_{19}$ are further integration constants.

3.2.5. Supernumerary Integration Constants

In the obtained analytical solution, nineteen integration constants appear. However, seven of them are supernumerary as a consequence of the adopted solution strategy (see Section 3.1). To determine the supernumerary integration constants, we substitute the solution for the interfacial stresses, Equation (18), and generalized displacements, Equations (26) and (27), into Equation (7). In this way, two identities are obtained, which need to be fulfilled for all values of x . The following seven relations among the integration constants are determined:

$$\begin{aligned}
 f_{10} &= - \frac{\alpha_3}{Bk_x \alpha_4} d_2 f_7, \quad f_{11} = \frac{\alpha_3}{Bk_x \alpha_4} d_1 f_7, \\
 f_{12} &= - \frac{(a_1 + b_1 h_1) d_2 - (b_2 - d_2 h_2) b_1}{\alpha_4} f_8 - \frac{a_2 d_2 - b_2^2}{\alpha_4} f_9, \\
 f_{13} &= \frac{a_1 d_1 - b_1^2}{\alpha_4} f_8 + \frac{(a_2 - b_2 h_2) d_1 - (b_1 + d_1 h_1) b_2}{\alpha_4} f_9, \\
 f_{14} &= f_{17} - (h_1 + h_2) f_{19} - \frac{1}{k_x} \left[\frac{1}{B} + \frac{\alpha_3}{B \alpha_4} (c_1 d_2 - c_2 d_1) h_1 \right] f_7, \\
 f_{15} &= f_{18}, \quad \text{and} \quad f_{16} = f_{19} + \frac{\alpha_3}{Bk_x \alpha_4} (c_1 d_2 - c_2 d_1) f_7,
 \end{aligned} \tag{28}$$

where:

$$\alpha_4 = b_1d_2 - b_2d_1 + d_1d_2(h_1 + h_2). \tag{29}$$

The values of the remaining twelve independent integration constants (f_1, f_2, \dots, f_9 and $f_{17}, f_{18},$ and f_{19}) have to be determined by imposing the boundary conditions of the particular problem being solved. It can be noted that the last three independent integration constants describe a rigid motion of the specimen and can be assessed only when appropriate kinematic restraints are prescribed. The adopted solution strategy enables the determination of the internal forces, strain measures, and relative displacements, even though the values of the last three constants remain undetermined.

3.3. Unbalanced Case

3.3.1. Interfacial Stresses

In the unbalanced case, Equations (14) are coupled. To separate the unknowns, we solve the first of such equations w.r.t. to $d\tau / dx$ and substitute the result into the second equation. After some simplifications, we obtain:

$$\begin{aligned} \frac{d^6\sigma}{dx^6} - \beta_1 \frac{d^4\sigma}{dx^4} + \beta_2 \frac{d^2\sigma}{dx^2} - \beta_3\sigma &= 0, \\ \frac{d\tau}{dx} &= -\frac{1}{k_z\beta_0} \left(\frac{d^4\sigma}{dx^4} - \alpha_1 \frac{d^2\sigma}{dx^2} + \alpha_2\sigma \right), \end{aligned} \tag{30}$$

where:

$$\beta_1 = \alpha_1 + \alpha_3, \quad \beta_2 = \alpha_2 + \alpha_1\alpha_3, \quad \text{and} \quad \beta_3 = \alpha_2\alpha_3 - k_xk_z\beta_0^2, \tag{31}$$

with $\alpha_1, \alpha_2, \alpha_3,$ and β_0 already defined in Equations (15) and (16), respectively.

The general solution for the interfacial stresses in the unbalanced case can be written as follows:

$$\begin{aligned} \sigma(x) &= \frac{1}{B} \sum_{i=1}^6 g_i \exp(-\mu_i x), \\ \tau(x) &= -\frac{k_x\beta_0}{B} \sum_{i=1}^6 \frac{g_i \exp(-\mu_i x)}{\mu_i (\mu_i^2 - \alpha_3)} + \frac{g_7}{B}, \end{aligned} \tag{32}$$

where g_1, g_2, \dots, g_7 are integration constants and $\mu_1, \mu_2, \dots, \mu_6$ are the non-zero roots of the characteristic equation of the differential problem (30):

$$\mu^6 - \beta_1\mu^4 + \beta_2\mu^2 - \beta_3 = 0. \tag{33}$$

By substituting Equation (31) into (33), the latter can be rearranged as:

$$(\mu^2 - \lambda_1^2) (\mu^2 - \lambda_3^2) (\mu^2 - \lambda_5^2) + k_xk_z\beta_0^2 = 0, \tag{34}$$

where $\lambda_1, \lambda_3,$ and λ_5 are given by Equation (19). From Equation (34), it can be easily concluded that the roots of the characteristic equation for the unbalanced case are different from those for the balanced case. Conversely, by assuming $\beta_0 = 0,$ Equation (34) turns out to be equivalent to Equation (20).

In general, Equation (33) can be solved numerically. In Appendix B.2, the conditions are given for which $\mu_1, \mu_2, \dots, \mu_6$ are real, along with their analytical expressions in this case. It should be noted that, strictly speaking, the solution expressed by Equation (32) is valid only when the characteristic equation has no coincident roots, which is the case for common geometric and material properties.

3.3.2. Internal Forces

By substituting Equation (32) into (9), the latter into (8), and integrating with respect to x , we obtain the expressions for the internal forces in the upper sublamine,

$$\begin{aligned}
 N_1(x) &= -k_x \beta_0 \sum_{i=1}^6 \frac{g_i}{\mu_i^2 (\mu_i^2 - \alpha_3)} \exp(-\mu_i x) - g_7 x - g_8, \\
 Q_1(x) &= \sum_{i=1}^6 \frac{g_i}{\mu_i} \exp(-\mu_i x) - g_{10}, \quad \text{and} \\
 M_1(x) &= -\sum_{i=1}^6 \frac{g_i}{\mu_i^2} \left(1 + \frac{h_1 k_x \beta_0}{\mu_i^2 - \alpha_3} \right) \exp(-\mu_i x) - (h_1 g_7 + g_{10}) x - g_{12},
 \end{aligned}
 \tag{35}$$

and in the lower sublamine,

$$\begin{aligned}
 N_2(x) &= k_x \beta_0 \sum_{i=1}^6 \frac{g_i}{\mu_i^2 (\mu_i^2 - \alpha_3)} \exp(-\mu_i x) + g_7 x + g_9, \\
 Q_2(x) &= -\sum_{i=1}^6 \frac{g_i}{\mu_i} \exp(-\mu_i x) + g_{11}, \quad \text{and} \\
 M_2(x) &= \sum_{i=1}^6 \frac{g_i}{\mu_i^2} \left(1 - \frac{h_2 k_x \beta_0}{\mu_i^2 - \alpha_3} \right) \exp(-\mu_i x) - (h_2 g_7 - g_{11}) x + g_{13},
 \end{aligned}
 \tag{36}$$

where g_8, g_9, \dots, g_{13} are integration constants.

3.3.3. Strain Measures

By substituting Equations (35) and (36) into (4), we obtain the expressions for the strain measures in the upper sublamine,

$$\begin{aligned}
 \epsilon_1(x) &= -\sum_{i=1}^6 \frac{g_i}{\mu_i^2} \left[\frac{k_x \beta_0}{\mu_i^2 - \alpha_3} (a_1 + b_1 h_1) + b_1 \right] \exp(-\mu_i x) + \\
 &\quad - [(a_1 + b_1 h_1) g_7 + b_1 g_{10}] x - a_1 g_8 - b_1 g_{12}, \\
 \gamma_1(x) &= c_1 \sum_{i=1}^6 \frac{g_i}{\mu_i} \exp(-\mu_i x) - c_1 g_{10}, \quad \text{and} \\
 \kappa_1(x) &= -\sum_{i=1}^6 \frac{g_i}{\mu_i^2} \left[d_1 + \frac{k_x \beta_0}{\mu_i^2 - \alpha_3} (d_1 h_1 + b_1) \right] \exp(-\mu_i x) + \\
 &\quad - [(d_1 h_1 + b_1) g_7 + d_1 g_{10}] x - b_1 g_8 - d_1 g_{12},
 \end{aligned}
 \tag{37}$$

and in the lower sublamine,

$$\begin{aligned}
 \epsilon_2(x) &= \sum_{i=1}^6 \frac{g_i}{\mu_i^2} \left[\frac{k_x \beta_0}{\mu_i^2 - \alpha_3} (a_2 - b_2 h_2) + b_2 \right] \exp(-\mu_i x) + \\
 &\quad + [(a_2 - b_2 h_2) g_7 + b_2 g_{11}] x + a_2 g_9 + b_2 g_{13}, \\
 \gamma_2(x) &= -c_2 \sum_{i=1}^6 \frac{g_i}{\mu_i} \exp(-\mu_i x) + c_2 g_{11}, \quad \text{and} \\
 \kappa_2(x) &= \sum_{i=1}^6 \frac{g_i}{\mu_i^2} \left[d_2 - \frac{k_x \beta_0}{\mu_i^2 - \alpha_3} (d_2 h_2 - b_2) \right] \exp(-\mu_i x) + \\
 &\quad - [(d_2 h_2 - b_2) g_7 - d_2 g_{11}] x + b_2 g_9 + d_2 g_{13}.
 \end{aligned}
 \tag{38}$$

3.3.4. Generalized Displacements

Lastly, by substituting Equations (37) and (38) into (1) and integrating the latter with respect to x , we obtain the expressions for the generalized displacements in the upper sublamine,

$$\begin{aligned}
 u_1(x) &= \sum_{i=1}^6 \frac{g_i}{\mu_i^3} \left[\frac{k_x \beta_0}{\mu_i^2 - \alpha_3} (a_1 + b_1 h_1) + b_1 \right] \exp(-\mu_i x) + \\
 &\quad - [(a_1 + b_1 h_1) g_7 + b_1 g_{10}] \frac{x^2}{2} - (a_1 g_8 + b_1 g_{12}) x + g_{14}, \\
 w_1(x) &= \sum_{i=1}^6 \frac{g_i}{\mu_i^2} \left[\frac{d_1}{\mu_i^2} - c_1 + \frac{k_x \beta_0 (d_1 h_1 + b_1)}{\mu_i^2 (\mu_i^2 - \alpha_3)} \right] \exp(-\mu_i x) + \\
 &\quad + [(d_1 h_1 + b_1) g_7 + d_1 g_{10}] \frac{x^3}{6} + (b_1 g_8 + d_1 g_{12}) \frac{x^2}{2} - (c_1 g_{10} + g_{16}) x + g_{15}, \quad \text{and} \\
 \varphi_1(x) &= \sum_{i=1}^6 \frac{g_i}{\mu_i^3} \left[\frac{k_x \beta_0}{\mu_i^2 - \alpha_3} (d_1 h_1 + b_1) + d_1 \right] \exp(-\mu_i x) + \\
 &\quad - [(d_1 h_1 + b_1) g_7 + d_1 g_{10}] \frac{x^2}{2} - (b_1 g_8 + d_1 g_{12}) x + g_{16},
 \end{aligned} \tag{39}$$

and in the lower sublamine,

$$\begin{aligned}
 u_2(x) &= - \sum_{i=1}^6 \frac{g_i}{\mu_i^3} \left[\frac{k_x \beta_0}{\mu_i^2 - \alpha_3} (a_2 - b_2 h_2) + b_2 \right] \exp(-\mu_i x) + \\
 &\quad + [(a_2 - b_2 h_2) g_7 + b_2 g_{11}] \frac{x^2}{2} + (a_2 g_9 + b_2 g_{13}) x + g_{17}, \\
 w_2(x) &= - \sum_{i=1}^6 \frac{g_i}{\mu_i^2} \left[\frac{d_2}{\mu_i^2} - c_2 - \frac{k_x \beta_0 (d_2 h_2 - b_2)}{\mu_i^2 (\mu_i^2 - \alpha_3)} \right] \exp(-\mu_i x) + \\
 &\quad + [(d_2 h_2 - b_2) g_7 - d_2 g_{11}] \frac{x^3}{6} - (b_2 g_9 + d_2 g_{13}) \frac{x^2}{2} + (c_2 g_{11} - g_{19}) x + g_{18}, \quad \text{and} \\
 \varphi_2(x) &= \sum_{i=1}^6 \frac{g_i}{\mu_i^3} \left[\frac{k_x \beta_0}{\mu_i^2 - \alpha_3} (d_2 h_2 - b_2) - d_2 \right] \exp(-\mu_i x) + \\
 &\quad - [(d_2 h_2 - b_2) g_7 - d_2 g_{11}] \frac{x^2}{2} + (b_2 g_9 + d_2 g_{13}) x + g_{19},
 \end{aligned} \tag{40}$$

where $g_{14}, g_{15}, \dots, g_{19}$ are further integration constants.

3.3.5. Supernumerary Integration Constants

As for the balanced case (see Section 3.2.5), nineteen integration constants appear in the analytical solution for the unbalanced case. Again, seven of them are supernumerary and can be determined by substituting the solution for the interfacial stresses, Equation (32), and generalized displacements, Equations (39) and (40), into Equation (7). In this way, two identities are obtained, which need to be fulfilled for all values of x . Consequently, the following seven relations among the integration constants are determined:

$$\begin{aligned}
 g_{10} &= \left(-\frac{\alpha_3}{Bk_x \alpha_4} d_2 + \beta_0 \frac{b_2 - d_2 h_2}{B\alpha_4} \right) g_7, \quad g_{11} = \left(\frac{\alpha_3}{Bk_x \alpha_4} d_1 - \beta_0 \frac{b_1 + d_1 h_1}{B\alpha_4} \right) g_7, \\
 g_{12} &= -\frac{(a_1 + b_1 h_1) d_2 - (b_2 - d_2 h_2) b_1}{\alpha_4} g_8 - \frac{a_2 d_2 - b_2^2}{\alpha_4} g_9, \\
 g_{13} &= \frac{a_1 d_1 - b_1^2}{\alpha_4} g_8 + \frac{(a_2 - b_2 h_2) d_1 - (b_1 + d_1 h_1) b_2}{\alpha_4} g_9, \\
 g_{14} &= g_{17} - (h_1 + h_2) g_{19} - \left[\frac{1}{Bk_x} + \frac{\alpha_3}{Bk_x \alpha_4} (c_1 d_2 - c_2 d_1) h_1 + \beta_0 \frac{b_1 c_2 - c_1 b_2 + c_1 d_2 h_2 + c_2 d_1 h_1}{B\alpha_4} h_1 \right] g_7, \\
 g_{15} &= g_{18}, \quad \text{and} \quad g_{16} = g_{19} + \left[\frac{\alpha_3}{Bk_x \alpha_4} (c_1 d_2 - c_2 d_1) + \beta_0 \frac{b_1 c_2 - c_1 b_2 + c_1 d_2 h_2 + c_2 d_1 h_1}{B\alpha_4} \right] g_7,
 \end{aligned} \tag{41}$$

where α_4 is furnished by Equation (29).

The values of the remaining twelve independent integration constants (g_1, g_2, \dots, g_9 and $g_{17}, g_{18},$ and g_{19}) have to be determined by imposing the boundary conditions of the particular problem being solved. Again, the last three independent integration constants describe a rigid motion of the specimen and can be assessed only when appropriate kinematic restraints are prescribed. The adopted solution strategy enables the determination of internal forces, strain measures, and relative displacements, even though the values of the last three constants remain undetermined.

4. Delamination Crack Analysis

4.1. Energy Release Rate

Under I/II mixed-mode fracture conditions, the *energy release rate* can be written as $\mathcal{G} = \mathcal{G}_I + \mathcal{G}_{II}$, where \mathcal{G}_I and \mathcal{G}_{II} are the contributions related to Fracture Modes I and II, respectively. In LEFM, the energy release rate identifies the path-independent \mathcal{J} -integral introduced by Rice [57]. Choosing an integration path encircling the interface between sublaminates, as detailed in Appendix C, we obtain:

$$\mathcal{J} = \frac{1}{2}k_z \Delta w^2(0) + \frac{1}{2}k_x \Delta u^2(0) \tag{42}$$

or, by recalling Equation (5),

$$\mathcal{J} = \frac{\sigma_0^2}{2k_z} + \frac{\tau_0^2}{2k_x}, \tag{43}$$

where $\sigma_0 = \sigma(0)$ and $\tau_0 = \tau(0)$ are the peak values of the interfacial stresses at the delamination front. The two addends in Equation (43) correspond to the Mode I and Mode II contributions to the energy release rate, respectively [41]. Since compressive normal stresses at the crack tip ($\sigma_0 < 0$) do not promote crack opening, the modal contributions to the energy release rate can be written as

$$\mathcal{G}_I = \mathcal{H}(\sigma_0) \frac{\sigma_0^2}{2k_z} \quad \text{and} \quad \mathcal{G}_{II} = \frac{\tau_0^2}{2k_x}, \tag{44}$$

where $\mathcal{H}(\cdot)$ denotes the Heaviside step function. By substituting Equation (18) into (44), we obtain the following expressions for the balanced case:

$$\mathcal{G}_I = \frac{\mathcal{H}(\sigma_0)}{2k_z B^2} \left(\sum_{i=1}^4 f_i \right)^2 \quad \text{and} \quad \mathcal{G}_{II} = \frac{1}{2k_x B^2} (f_5 + f_6)^2. \tag{45}$$

Likewise, by substituting Equation (32) into (44), we obtain the following expressions for the unbalanced case:

$$\mathcal{G}_I = \frac{\mathcal{H}(\sigma_0)}{2k_z B^2} \left(\sum_{i=1}^6 g_i \right)^2 \quad \text{and} \quad \mathcal{G}_{II} = \frac{1}{2k_x B^2} \left(k_x \beta_0 \sum_{i=1}^6 \frac{g_i}{\mu_i (\mu_i^2 - \alpha_3)} \right)^2. \tag{46}$$

Lastly, to characterize the ratio between the modal contributions to the energy release rate, we introduce the *mode-mixity angle* [11],

$$\psi = \text{sign}(\tau_0) \arctan \sqrt{\frac{\mathcal{G}_{II}}{\mathcal{G}_I}}, \tag{47}$$

ranging from 0° (pure Mode I) to 90° (pure Mode II).

5. Results

5.1. Examples

By way of illustration, we applied the developed solution to the analysis of the DCB test (Figure 3). Laminated specimens with the following geometric sizes were considered: $L = 100$ mm, $B = 25$ mm, and $H = 3.2$ mm. A delamination length $a = 25$ mm and a reference load $P = 100$ N were used in all of the following calculations. Boundary conditions (12) and (13) were specialized to the present case by taking the crack tip internal forces as $N_1^A = N_2^A = 0$, $Q_1^A = -Q_2^A = P$, and $M_1^A = -M_2^A = Pa$ and assuming a CTE length $\ell = L - a$.

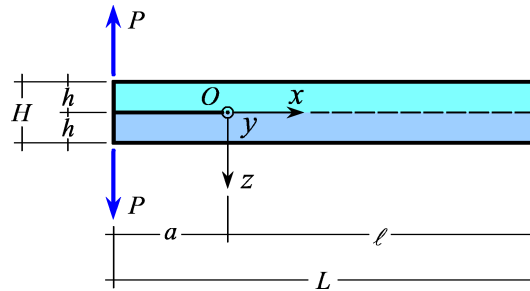


Figure 3. Double cantilever beam test.

Three laminated specimens with different stacking sequences were ideally built as follows. We started from a typical carbon-epoxy fiber-reinforced lamina of thickness $t_p = 0.2$ mm and elastic moduli shown in Table 1 [61]. Based on this, three stacking sequences were designed corresponding to uni-directional (UD), cross-ply (CP), and multi-directional (MD) sublaminates (Table 2). Lastly, the DCB test specimens were obtained by variously assembling the sublaminates one over the other:

- UD//UD
- UD//CP
- UD//MD

where the double slash (//) represents the position of the delamination crack.

Table 1. Lamina elastic moduli.

E_1 (MPa)	$E_2 = E_3$ (MPa)	$\nu_{12} = \nu_{13}$ -	ν_{23} -	$G_{12} = G_{13}$ (MPa)	G_{23} (MPa)
109,000	8819	0.342	0.380	4315	3200

Table 2. Sublaminates stacking sequences.

Sublaminates	Stacking Sequence
UD	$[0^{\circ}_8]$
CP	$[0^{\circ}/90^{\circ}/0^{\circ}_2/90^{\circ}_3/0^{\circ}]$
MD	$[45^{\circ}/-45^{\circ}_2/90^{\circ}/45^{\circ}_2/-45^{\circ}/0^{\circ}]$

The sublaminates plate stiffness matrices, calculated as explained in Appendix A, are reported in Table 3. It can be noted that no bending-extension coupling was exhibited by the UD sublaminates (all terms $B_{ij} = 0$), while bending-extension coupling was shown by both the CP (terms $B_{xx} = -B_{yy} \neq 0$) and MD sublaminates (all terms $B_{ij} \neq 0$, except $B_{xs} = B_{ys} = 0$).

Table 3. Sublaminates plate stiffnesses.

Sublaminates	$[A_{ij}]$ (N/mm)			$[B_{ij}]$ (N)			$[D_{ij}]$ (N mm)		
UD	176,066	4872	0	0	0	0	37,561	1039	0
	4872	14,245	0	0	0	0	1039	3039	0
	0	0	6904	0	0	0	0	0	1473
CP	95,156	4872	0	8091	0	0	25,155	1039	0
	4872	95,156	0	0	-8091	0	1039	15,445	0
	0	0	6904	0	0	0	0	0	1473
MD	66,477	33,550	0	10,959	-2868	0	19,419	6775	0
	33,550	66,477	0	-2868	-5223	0	6775	9710	0
	0	0	35,582	0	0	-2868	0	0	7209

The sublaminates equivalent beam stiffnesses, calculated via Equations (A10) and (A19), are given in Table 4. It can be noted that the UD sublaminates had the highest extensional and bending stiffnesses, A and D, while the MD sublaminates had the highest bending-extension coupling stiffness, B. The shear stiffness, C, showed little variations among the chosen stacking sequences.

Table 4. Sublaminates equivalent beam stiffnesses.

Sublaminates	A (kN)	B (kN mm)	C (kN)	D (kN mm ²)
UD	4360.0	0	143.8	930.1
CP	2372.4	201.5	129.0	627.0
MD	1238.5	314.2	123.8	367.0

A crucial point for the successful implementation of the present model is the appropriate choice of the values of the elastic interface constants. These can be assigned by conducting a compliance calibration with experimental tests or numerical simulations, if available [62]. In a previous study on asymmetric DCB test specimens [22], compliance calibration with finite element simulations gave:

$$k_x \approx 16.2 \frac{G_{13}}{H} \quad \text{and} \quad k_z \approx 6.9 \frac{E_3}{H}, \tag{48}$$

which, in the present case, yielded $k_x = 21,845 \text{ N/mm}^3$ and $k_z = 19,016 \text{ N/mm}^3$. Such values were adopted for the present examples.

Figure 4 shows the plots of the interfacial stresses and internal forces as functions of the x -coordinate in the neighborhood of the crack tip for the UD//UD specimen. This specimen was symmetric; hence, the unbalance parameter was $\beta_0 = 0$, and the analytical solution for the balanced case applied (see Section 3.2). For the DCB test, the specimen response also corresponded to pure Mode I fracture conditions: actually, Figure 4a shows that the shear stresses were identically null, while the normal stresses attained a peak value at the crack tip cross-section. Figure 4b shows that also the sublaminates axial forces were null. Instead, Figure 4c,d shows the trends of the sublaminates shear forces and bending moments, which started from the assigned values at the crack tip cross-section and then approached zero asymptotically. Shear forces and bending moments had symmetric trends in the upper and lower sublaminates because of the specimen symmetry.

Figures 5 and 6 show the plots of the interfacial stresses and internal forces as functions of the x -coordinate in the neighborhood of the crack tip for the UD//CP and UD//MD specimens, respectively. Both specimens were asymmetric with unbalance parameter $\beta_0 \neq 0$. Hence, the analytical solution for the unbalanced case applied (see Section 3.3). For the DCB test, the specimen response corresponded to I/II mixed-mode fracture conditions: actually, both Figures 5a and 6a show non-zero

normal and shear stresses, which attained peak values at the crack tip cross-section. All of the internal forces started from the assigned values at the crack tip cross-section and then approached zero asymptotically.

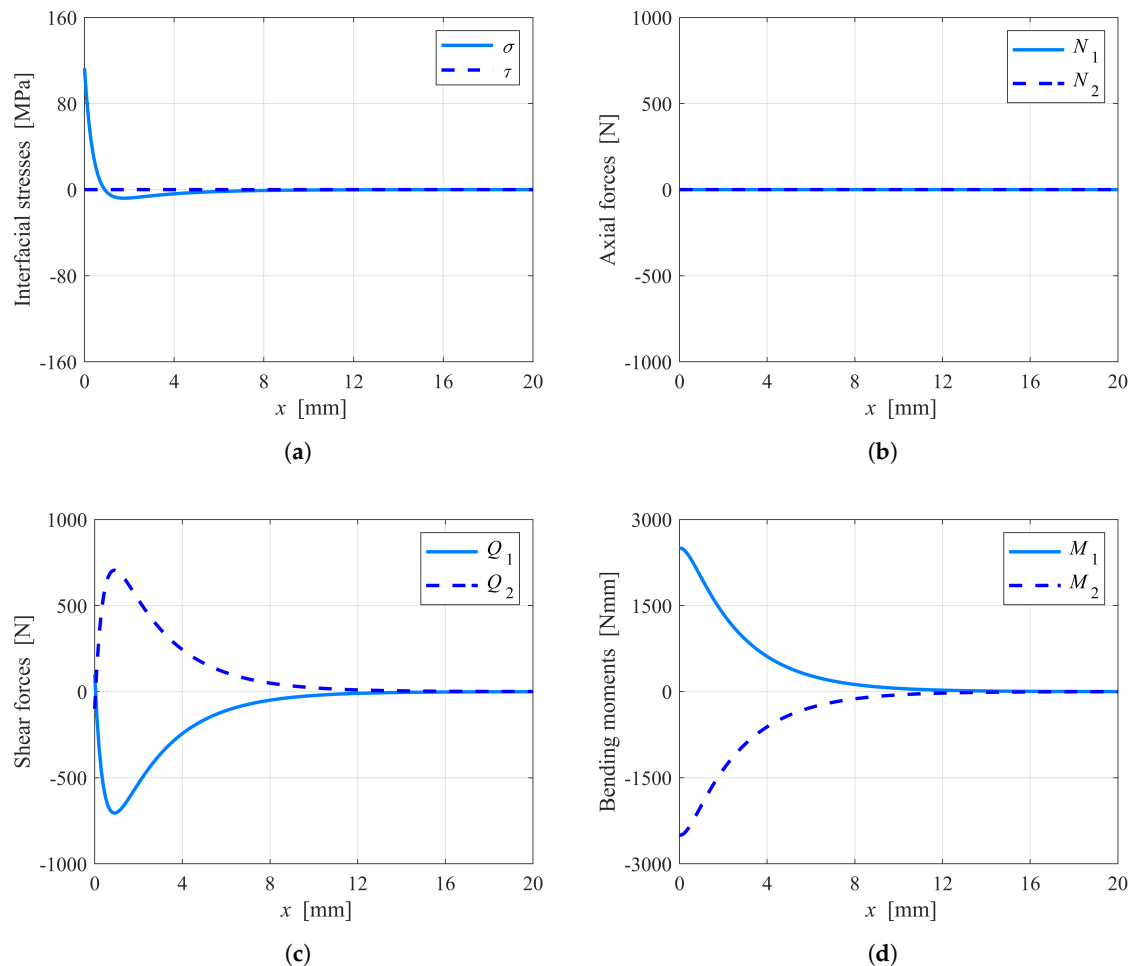


Figure 4. UD//UD specimen: (a) interfacial stresses, (b) axial forces, (c) shear forces, and (d) bending moments in the crack tip neighborhood.

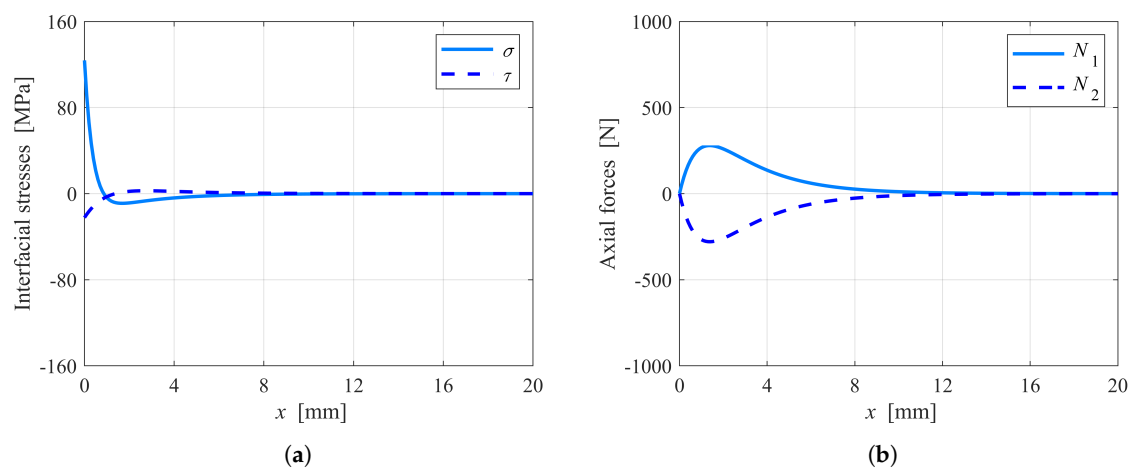


Figure 5. Cont.

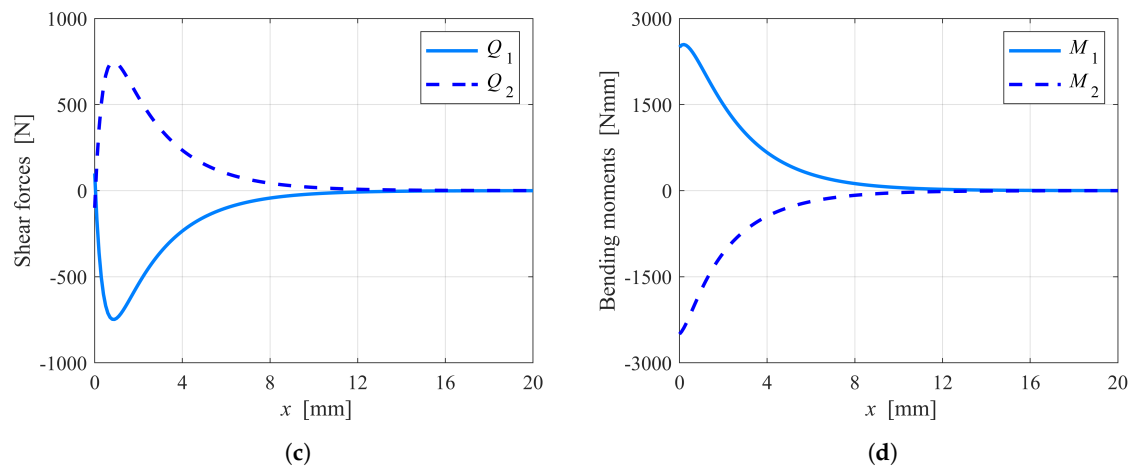


Figure 5. UD//CP specimen: (a) interfacial stresses, (b) axial forces, (c) shear forces, and (d) bending moments in the crack tip neighborhood.

Table 5 reports the Mode I and II contributions to the energy release rate computed for the three analyzed specimens, along with the total energy release rate and mode-mixity angle. It is apparent that the relative amount of the Mode II contribution increased with the specimen asymmetry.

Table 5. Energy release rate and mode mixity.

Specimen	\mathcal{G}_I (J/m ²)	\mathcal{G}_{II} (J/m ²)	\mathcal{G} (J/m ²)	ψ (deg)
UD//UD	339.7	0	339.7	0
UD//CP	403.4	11.4	414.8	−9.5
UD//MD	524.2	135.9	660.1	−27.0

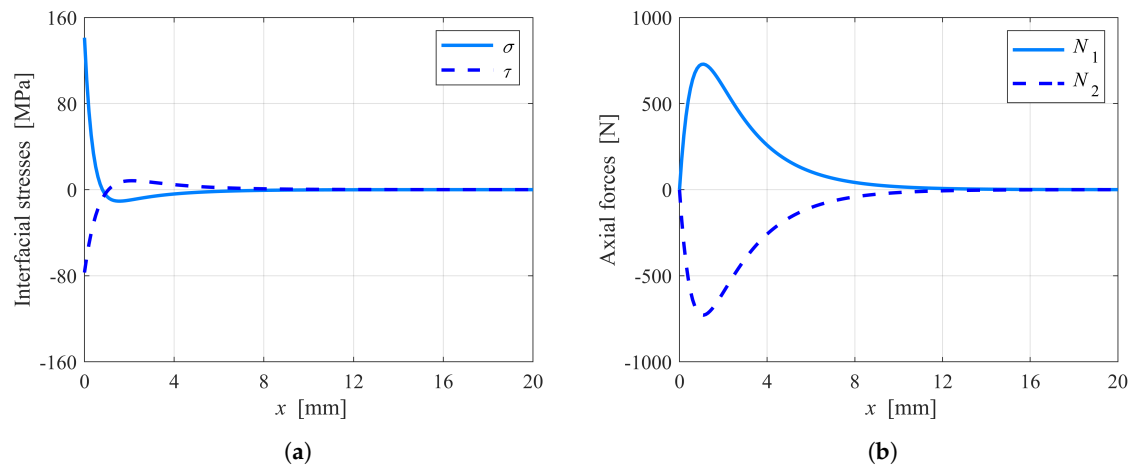


Figure 6. Cont.

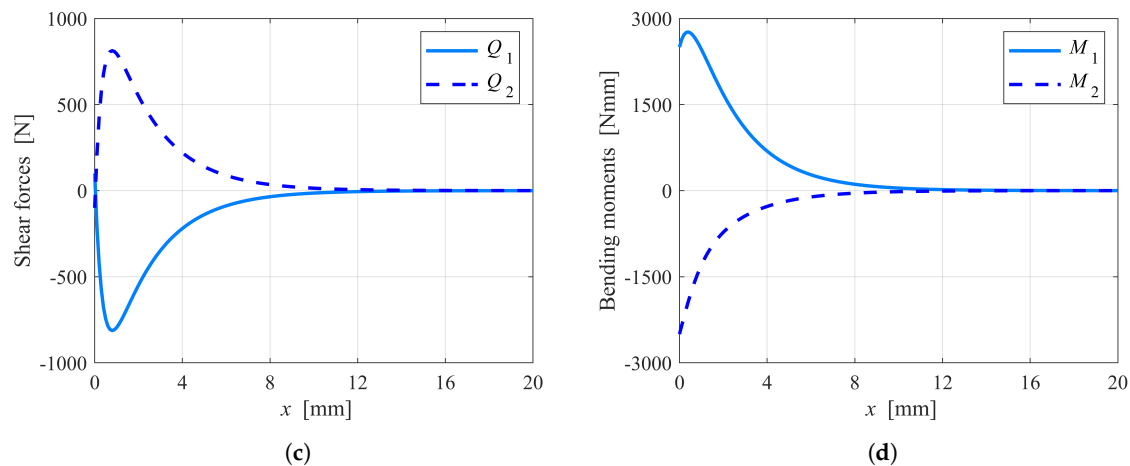


Figure 6. UD//MD specimen: (a) interfacial stresses, (b) axial forces, (c) shear forces, and (d) bending moments in the crack tip neighborhood.

5.2. Effects of Interface Stiffness

Figure 7 shows a schematic of the double cantilever beam specimen loaded by uneven bending moments (DCB-UBM) test [63]. Here, this particular test configuration was used to illustrate the effects of interface stiffness, i.e., of the values of the interface elastic constants, k_x and k_z , on the solution according to the proposed model.

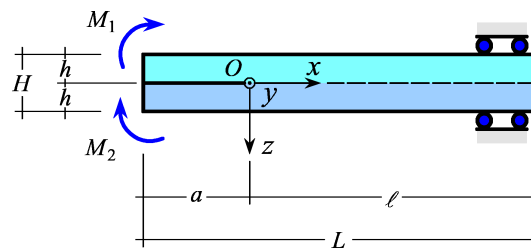
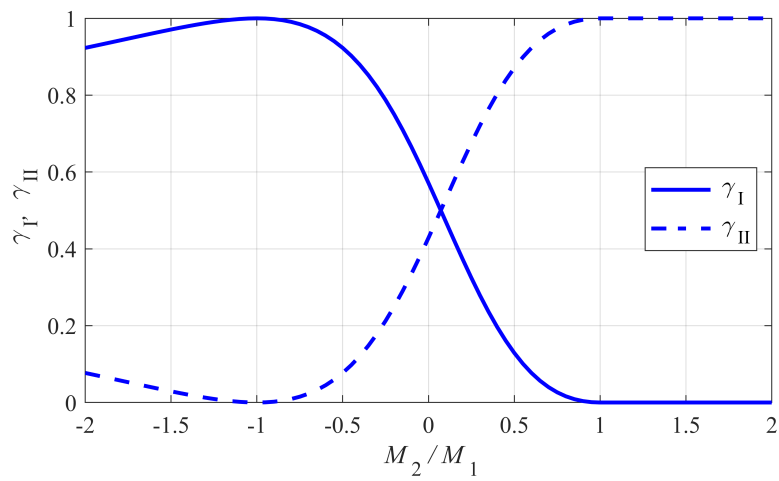


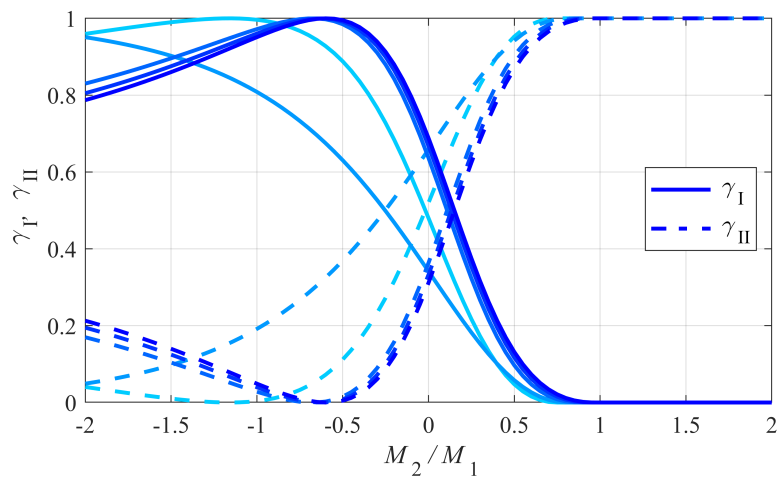
Figure 7. Double cantilever beam specimen with uneven bending moments.

The same laminated specimens considered in the examples of Section 5.1 were again analyzed, but subjected to different loading conditions. The upper sublaminar was loaded by a unit bending couple, $M_1 = 1$ N m, while the lower sublaminar was loaded by a variable bending couple, M_2 . Figure 8 shows the dimensionless Mode I and Mode II contributions to the energy release rate, $\gamma_I = G_I/G$ and $\gamma_{II} = G_{II}/G$, as functions of the bending moment ratio, M_2/M_1 .

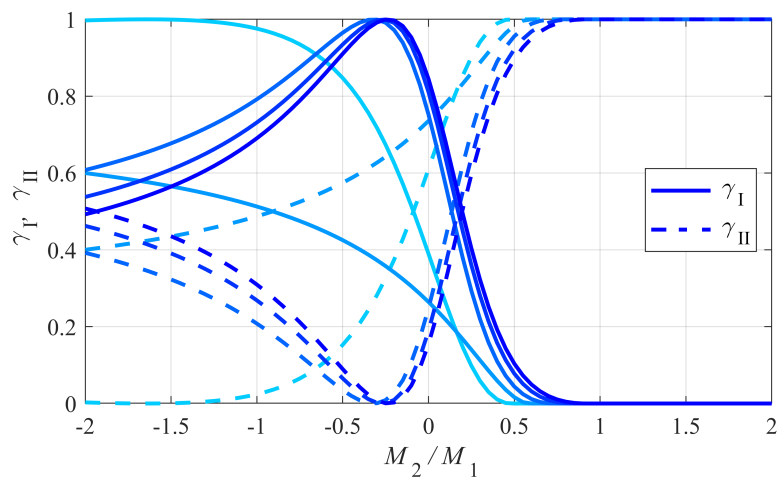
For the UD//UD specimen (Figure 8a), the modal contributions to G turned out to be independent of the interface stiffness. This result was due to the mid-plane symmetry of the specimen and the independence of the crack tip bending moments on the delamination length. In this case, also the mode mixity depended uniquely on the bending moment ratio, M_2/M_1 . In particular, it can be noted how pure Mode I fracture conditions ($\gamma_{II} = 0$) were obtained for $M_2 = -M_1$, while pure Mode II fracture conditions ($\gamma_I = 0$) were obtained for $M_2 = M_1$. Values of M_2/M_1 greater than one also corresponded to pure Mode II because of the incompressibility constraint introduced for G_I in Equation (44).



(a)



(b)



(c)

Figure 8. Dimensionless modal contributions to energy release rate vs. sublaminar bending moment ratio: (a) UD//UD specimen, (b) UD//CP specimen, and (c) UD//MD specimen.

Instead, for both the UD//CP (Figure 8b) and UD//MD specimens (Figure 8c), the modal contributions to \mathcal{G} depended on the values of the interface elastic constants, k_x and k_z . For each modal contribution, the plots show five curves with different shades of blue: from lighter to darker, and these correspond to $k_x = k_z = 10^2, 10^3, 10^4$, and 10^5 N/mm³; the darkest curves represent the limit case $k_x = k_z \rightarrow +\infty$, which corresponds to a rigid interface model [51]. For the specimens considered, also the mode mixity and the conditions for pure fracture modes depended on the interface stiffness.

The range of values adopted for k_x and k_z in the previous plots may look quite wide. Indeed, this range corresponds to real values that may be obtained when performing a compliance calibration with experimental results or numerical simulations [62]. The results obtained suggest that the elastic interface model is potentially capable of highly-accurate prediction and interpretation of experimental results, provided that the appropriate values of the interface elastic constants are selected. To this aim, it would be useful to validate the theoretical predictions obtained with experimental results, such as those obtained by Davidson et al. [64,65]. Such a comparison, similar to the one carried out by Harvey et al. to validate different mixed-mode partition theories [66,67], will be the subject of future work.

6. Conclusions

An elastic interface model was introduced for the analysis of delamination in bending-extension coupled laminated beams with through-the-width delamination cracks. The analytical solution obtained applies to a wide class of multi-directional fiber-reinforced composite laminates, including cross-ply laminates, provided that their stacking sequences allow them to be modeled as plane beams. Examples illustrated the application of the model to the analysis of the double cantilever beam test in I/II mixed-mode fracture conditions. Furthermore, the effects of the interface stiffness on the model predictions were discussed with reference to the DCB specimen loaded with uneven bending moments.

By suitably adapting the boundary conditions, the outlined solution can be easily used to analyze different delamination toughness test configurations, as well as delamination behavior in real structural elements and debonding of adhesively-bonded joints.

The proposed model is potentially capable of highly-accurate prediction and interpretation of experimental results, provided that the appropriate interface stiffness is defined. In this respect, it will be useful to compare the model predictions with the results of experimental tests available in the literature. Future developments also include the extension of the model to fully-coupled laminates, for which plate theory must be used, and I/II/III mixed-mode fracture conditions are expected.

Author Contributions: Conceptualization, S.B., P.F., L.T., and P.S.V.; methodology, S.B., P.F., L.T., and P.S.V.; software, P.F. and P.S.V.; validation, P.S.V.; formal analysis, P.F. and L.T.; investigation, P.F. and L.T.; resources, S.B. and P.S.V.; data curation, P.F. and P.S.V.; writing, original draft preparation, P.F., L.T. and P.S.V.; writing, review and editing, S.B.; visualization, P.F. and P.S.V.; supervision, S.B.; project administration, P.S.V.; funding acquisition, S.B. and P.S.V.

Funding: This research received no external funding.

Conflicts of Interest: The authors declare no conflict of interest.

Abbreviations

The following abbreviations are used in this manuscript:

CTE	crack-tip element
CP	cross-ply
DCB	double cantilever beam
DCB-UBM	double cantilever beam with uneven bending moments
LEFM	linear elastic fracture mechanics
MD	multi-directional
UD	uni-directional

Appendix A. Laminated Beam Stiffnesses

For a homogenous and special orthotropic beam of width B and thickness H , the extensional, bending-coupling, shear, and bending stiffnesses can be calculated respectively as:

$$A = E_x BH, \quad B = 0, \quad C = \frac{5}{6} G_{zx} BH, \quad \text{and} \quad D = \frac{1}{12} E_x BH^3, \quad (A1)$$

where E_x and G_{zx} respectively are the longitudinal Young's modulus and the transverse shear modulus of the material.

For laminated beams with generic stacking sequences, the above quantities have to be calculated as explained in the following sections.

Appendix A.1. Extension and Bending Stiffnesses

For a laminated plate with a generic stacking sequence, the constitutive laws are:

$$\begin{Bmatrix} N_x \\ N_y \\ N_{xy} \end{Bmatrix} = \begin{bmatrix} A_{xx} & A_{xy} & A_{xs} \\ A_{xy} & A_{yy} & A_{ys} \\ A_{xs} & A_{ys} & A_{ss} \end{bmatrix} \begin{Bmatrix} \epsilon_x \\ \epsilon_y \\ \gamma_{xy} \end{Bmatrix} + \begin{bmatrix} B_{xx} & B_{xy} & B_{xs} \\ B_{xy} & B_{yy} & B_{ys} \\ B_{xs} & B_{ys} & B_{ss} \end{bmatrix} \begin{Bmatrix} \kappa_x \\ \kappa_y \\ \kappa_{xy} \end{Bmatrix} \quad (A2)$$

and:

$$\begin{Bmatrix} M_x \\ M_y \\ M_{xy} \end{Bmatrix} = \begin{bmatrix} B_{xx} & B_{xy} & B_{xs} \\ B_{xy} & B_{yy} & B_{ys} \\ B_{xs} & B_{ys} & B_{ss} \end{bmatrix} \begin{Bmatrix} \epsilon_x \\ \epsilon_y \\ \gamma_{xy} \end{Bmatrix} + \begin{bmatrix} D_{xx} & D_{xy} & D_{xs} \\ D_{xy} & D_{yy} & D_{ys} \\ D_{xs} & D_{ys} & D_{ss} \end{bmatrix} \begin{Bmatrix} \kappa_x \\ \kappa_y \\ \kappa_{xy} \end{Bmatrix}, \quad (A3)$$

where N_x , N_y , and N_{xy} are the in-plane forces and M_x , M_y , and M_{xy} are the bending moments (per unit plate width); correspondingly, ϵ_x , ϵ_y , and γ_{xy} are the in-plane strains and κ_x , κ_y , and κ_{xy} are the bending curvatures; A_{ij} , B_{ij} , and D_{ij} , with $i, j \in \{x, y, s\}$, are the coefficients of the extensional, bending-extension coupling, and bending stiffness matrices, respectively, to be computed following classical laminated plate theory [49]:

$$\begin{Bmatrix} A_{ij} \\ B_{ij} \\ D_{ij} \end{Bmatrix} = \sum_{k=1}^n Q_{ij}^{(k)} \begin{Bmatrix} z_k - z_{k-1} \\ \frac{1}{2}(z_k^2 - z_{k-1}^2) \\ \frac{1}{3}(z_k^3 - z_{k-1}^3) \end{Bmatrix}, \quad (A4)$$

where $Q_{ij}^{(k)}$, with $i, j \in \{x, y, s\}$, are the in-plane elastic moduli of the k th lamina, included between the ordinates $z = z_{k-1}$ and $z = z_k$, in the global reference system, and n is the total number of laminae. For an orthotropic lamina, whose principal material axes, 1 and 2, are rotated by an angle θ_k with respect to the global axes x and y ,

$$\begin{aligned} Q_{xx}^{(k)} &= Q_{11}^{(k)} \cos^4 \theta_k + 2(Q_{12}^{(k)} + 2Q_{66}^{(k)}) \cos^2 \theta_k \sin^2 \theta_k + Q_{22}^{(k)} \sin^4 \theta_k, \\ Q_{xy}^{(k)} &= Q_{yx}^{(k)} = (Q_{11}^{(k)} + Q_{22}^{(k)} - 4Q_{66}^{(k)}) \cos^2 \theta_k \sin^2 \theta_k + Q_{12}^{(k)} (\cos^4 \theta_k + \sin^4 \theta_k), \\ Q_{xs}^{(k)} &= Q_{sx}^{(k)} = (Q_{11}^{(k)} - Q_{12}^{(k)} - 2Q_{66}^{(k)}) \cos^3 \theta_k \sin \theta_k + (Q_{12}^{(k)} - Q_{22}^{(k)} + 2Q_{66}^{(k)}) \cos \theta_k \sin^3 \theta_k, \\ Q_{yy}^{(k)} &= Q_{11}^{(k)} \sin^4 \theta_k + 2(Q_{12}^{(k)} + 2Q_{66}^{(k)}) \cos^2 \theta_k \sin^2 \theta_k + Q_{22}^{(k)} \cos^4 \theta_k, \\ Q_{ys}^{(k)} &= Q_{sy}^{(k)} = (Q_{11}^{(k)} - Q_{12}^{(k)} - 2Q_{66}^{(k)}) \cos \theta_k \sin^3 \theta_k + (Q_{12}^{(k)} - Q_{22}^{(k)} + 2Q_{66}^{(k)}) \cos^3 \theta_k \sin \theta_k, \quad \text{and} \\ Q_{ss}^{(k)} &= (Q_{11}^{(k)} + Q_{22}^{(k)} - 2Q_{12}^{(k)} - 2Q_{66}^{(k)}) \cos^2 \theta_k \sin^2 \theta_k + Q_{66}^{(k)} (\cos^4 \theta_k + \sin^4 \theta_k), \end{aligned} \quad (A5)$$

where the in-plane elastic moduli of the lamina in its principal material reference system are:

$$\begin{aligned}
 Q_{11}^{(k)} &= \frac{E_1^{(k)}}{1 - \nu_{12}^{(k)} \nu_{21}^{(k)}}, & Q_{12}^{(k)} = Q_{21}^{(k)} &= \frac{\nu_{12}^{(k)} E_2^{(k)}}{1 - \nu_{12}^{(k)} \nu_{21}^{(k)}}, \\
 Q_{22}^{(k)} &= \frac{E_2^{(k)}}{1 - \nu_{12}^{(k)} \nu_{21}^{(k)}}, & \text{and } Q_{66}^{(k)} &= G_{12}^{(k)}
 \end{aligned}
 \tag{A6}$$

with $E_1^{(k)}, E_2^{(k)}, \nu_{12}^{(k)}, \nu_{21}^{(k)}$, and $G_{12}^{(k)}$ being the in-plane elastic moduli of the lamina in engineering notation.

For a plate to be modeled as a plane beam in the zx -plane, the out-of-plane internal forces and moments must be $N_y = N_{xy} = 0$ and $M_y = M_{xy} = 0$. Besides, the shear-extension and bend-twist coupling terms must vanish: $A_{xs} = A_{ys} = 0$ and $D_{xs} = D_{ys} = 0$. The bending-shear coupling terms must also be null: $B_{xs} = B_{ys} = 0$. Such conditions are fulfilled by laminates with single or multiple special orthotropic layers and antisymmetric cross-ply laminates. Furthermore, antisymmetric angle-ply and generic multi-directional laminates may satisfy the above-mentioned conditions for particular stacking sequences. As a consequence, Equations (A2) and (A3) reduce to:

$$\begin{Bmatrix} N_x \\ 0 \\ 0 \end{Bmatrix} = \begin{bmatrix} A_{xx} & A_{xy} & 0 \\ A_{xy} & A_{yy} & 0 \\ 0 & 0 & A_{ss} \end{bmatrix} \begin{Bmatrix} \epsilon_x \\ \epsilon_y \\ \gamma_{xy} \end{Bmatrix} + \begin{bmatrix} B_{xx} & B_{xy} & 0 \\ B_{xy} & B_{yy} & 0 \\ 0 & 0 & B_{ss} \end{bmatrix} \begin{Bmatrix} \kappa_x \\ \kappa_y \\ \kappa_{xy} \end{Bmatrix}
 \tag{A7}$$

and:

$$\begin{Bmatrix} M_x \\ 0 \\ 0 \end{Bmatrix} = \begin{bmatrix} B_{xx} & B_{xy} & 0 \\ B_{xy} & B_{yy} & 0 \\ 0 & 0 & B_{ss} \end{bmatrix} \begin{Bmatrix} \epsilon_x \\ \epsilon_y \\ \gamma_{xy} \end{Bmatrix} + \begin{bmatrix} D_{xx} & D_{xy} & 0 \\ D_{xy} & D_{yy} & 0 \\ 0 & 0 & D_{ss} \end{bmatrix} \begin{Bmatrix} \kappa_x \\ \kappa_y \\ \kappa_{xy} \end{Bmatrix}.
 \tag{A8}$$

For a laminated beam of width B , the axial force and bending moment respectively are $N = BN_x$ and $M = BM_x$; the axial strain and pseudo-curvature are $\epsilon = \epsilon_x$ and $\kappa = \kappa_x$. Thus, from Equations (A7) and (A8), the constitutive laws are derived as follows:

$$N = A\epsilon + B\kappa \quad \text{and} \quad M = B\epsilon + D\kappa,
 \tag{A9}$$

where the laminated beam stiffnesses are evaluated as:

$$\begin{aligned}
 A &= B \left(A_{xx} - \frac{A_{xy}^2 D_{yy} - 2A_{xy} B_{xy} B_{yy} + A_{yy} B_{xy}^2}{A_{yy} D_{yy} - B_{yy}^2} \right), \\
 B &= B \left[B_{xx} + \frac{A_{xy} (B_{yy} D_{xy} - B_{xy} D_{yy}) - A_{yy} B_{xy} D_{xy} + B_{xy}^2 B_{yy}}{A_{yy} D_{yy} - B_{yy}^2} \right], \quad \text{and} \\
 D &= B \left(D_{xx} - \frac{A_{yy} D_{xy}^2 - 2B_{xy} B_{yy} D_{xy} + B_{xy}^2 D_{yy}}{A_{yy} D_{yy} - B_{yy}^2} \right),
 \end{aligned}
 \tag{A10}$$

and the remaining plate strain measures turn out to be:

$$\begin{aligned}
 \epsilon_y &= -\frac{A_{xy} D_{yy} - B_{xy} B_{yy}}{A_{yy} D_{yy} - B_{yy}^2} \epsilon - \frac{B_{xy} D_{yy} - B_{yy} D_{xy}}{A_{yy} D_{yy} - B_{yy}^2} \kappa, \\
 \gamma_{xy} &= 0, \\
 \kappa_y &= -\frac{A_{yy} B_{xy} - A_{xy} B_{yy}}{A_{yy} D_{yy} - B_{yy}^2} \epsilon - \frac{A_{yy} D_{xy} - B_{xy} B_{yy}}{A_{yy} D_{yy} - B_{yy}^2} \kappa, \quad \text{and} \\
 \kappa_{xy} &= 0.
 \end{aligned}
 \tag{A11}$$

Appendix A.2. Shear Stiffness

The shear stiffness of a laminated plate can be evaluated by imposing a strain energy equivalence, as usually done for homogeneous beams [56] and recently extended to laminated plates by Xie et al. [25]. Here, we detail such a procedure for a laminated beam [68–70]. To this aim, first we recall the expression of the normal stress in the x -direction within the k th lamina [49]:

$$\sigma_x^{(k)}(z) = Q_{xx}^{(k)} (\epsilon_x + z\kappa_x) + Q_{xy}^{(k)} (\epsilon_y + z\kappa_y) + Q_{xs}^{(k)} (\gamma_{xy} + z\kappa_{xy}). \tag{A12}$$

Next, we substitute the expressions of the plate strain measures obtained in the previous section into Equation (A12). Thus, we obtain:

$$\sigma_x^{(k)}(z) = Q_{\epsilon 0}^{(k)} \epsilon + Q_{\kappa 0}^{(k)} \kappa + z \left(Q_{\epsilon 1}^{(k)} \epsilon + Q_{\kappa 1}^{(k)} \kappa \right), \tag{A13}$$

where:

$$\begin{aligned} Q_{\epsilon 0}^{(k)} &= Q_{xx}^{(k)} - \frac{A_{xy}D_{yy} - B_{xy}B_{yy}}{A_{yy}D_{yy} - B_{yy}^2} Q_{xy}^{(k)}, & Q_{\kappa 0}^{(k)} &= -\frac{B_{xy}D_{yy} - B_{yy}D_{xy}}{A_{yy}D_{yy} - B_{yy}^2} Q_{xy}^{(k)}, \\ Q_{\epsilon 1}^{(k)} &= -\frac{A_{yy}B_{xy} - A_{xy}B_{yy}}{A_{yy}D_{yy} - B_{yy}^2} Q_{xy}^{(k)}, & \text{and } Q_{\kappa 1}^{(k)} &= Q_{xx}^{(k)} - \frac{A_{yy}D_{xy} - B_{xy}B_{yy}}{A_{yy}D_{yy} - B_{yy}^2} Q_{xy}^{(k)}. \end{aligned} \tag{A14}$$

Following the classical derivation of Jourawski’s shear stress formula [56], we impose the static equilibrium in the x -direction of a short portion of beam defined by a given value of the z -coordinate. Thus, by recalling the inverse constitutive Equation (4) and static equilibrium Equation (8), with no distributed loads, the following expression is obtained for the shear stress in the k th lamina:

$$\tau_{zx}^{(k)}(z) = Q \left(R_k - S_k z - T_k z^2 \right), \tag{A15}$$

where Q is the transverse shear force (acting in the z -direction) and:

$$\begin{aligned} R_k &= S_k z_k + T_k z_k^2 + \sum_{j=k+1}^n \left[S_j (z_j - z_{j-1}) + T_j (z_j^2 - z_{j-1}^2) \right], \\ S_k &= bQ_{\epsilon 0}^{(k)} + dQ_{\kappa 0}^{(k)}, & \text{and } T_k &= \frac{1}{2} \left(bQ_{\epsilon 1}^{(k)} + dQ_{\kappa 1}^{(k)} \right), \end{aligned} \tag{A16}$$

where b and d respectively are the bending-extension and bending compliances of the laminated beam, as given by Equation (3).

The shear compliance, c , can now be calculated by imposing the following energy equivalence for a short beam segment:

$$\frac{1}{2} c Q^2 = \frac{1}{2} B \int_{-h}^h \frac{1}{G_{zx}^{(k)}} \left[\tau_{zx}^{(k)}(z) \right]^2 dz, \tag{A17}$$

where:

$$G_{zx}^{(k)} = \frac{1}{\frac{\sin^2 \theta_k}{G_{23}^{(k)}} + \frac{\cos^2 \theta_k}{G_{31}^{(k)}}} \tag{A18}$$

is the transverse shear modulus of the k th lamina in the laminate reference system, depending on its out-of-plane shear moduli, $G_{23}^{(k)}$ and $G_{31}^{(k)}$. By substituting Equation (A15) into (A17), the shear compliance is obtained:

$$c = B \sum_{k=1}^n \frac{1}{G_{zx}^{(k)}} \left[R_k^2 (z_k - z_{k-1}) - R_k S_k (z_k^2 - z_{k-1}^2) + \frac{1}{3} (S_k^2 - 2R_k T_k) (z_k^3 - z_{k-1}^3) + \frac{1}{2} S_k T_k (z_k^4 - z_{k-1}^4) + \frac{1}{5} T_k^2 (z_k^5 - z_{k-1}^5) \right]. \tag{A19}$$

Lastly, the laminated beam shear stiffness is $C = 1/c$.

Appendix B. Properties of Characteristic Equation Roots

Appendix B.1. Balanced Case

The roots, $\lambda_1, \lambda_2, \dots, \lambda_6$, of the characteristic Equation (20) for the uncoupled differential problem are furnished by Equation (19). They attain real values if:

$$\alpha_1 > 2\sqrt{\alpha_2} \quad \text{and} \quad \alpha_3 > 0, \tag{A20}$$

that is, recalling the definitions of Equation (15),

$$k_x > 0, \quad k_z > \hat{k}_z, \quad \text{and} \quad a_1 + d_1 h_1^2 + a_2 + d_2 h_2^2 > 2b_2 h_2 - 2b_1 h_1, \tag{A21}$$

with \hat{k}_z introduced by Equation (21). The above conditions are usually fulfilled for geometric and material properties corresponding to common fiber-reinforced laminates.

Appendix B.2. Unbalanced Case

The roots, $\mu_1, \mu_2, \dots, \mu_6$, of the characteristic Equation (33) for the coupled differential problem can be computed numerically. They attain distinct real values if the associated cubic equation has positive discriminant,

$$D = \beta_1^2 \beta_2^2 - 4\beta_2^3 - 4\beta_1^3 \beta_3 + 18\beta_1 \beta_2 \beta_3 - 27\beta_3^2 > 0, \tag{A22}$$

and positive roots,

$$\begin{aligned} \zeta_1 &= \frac{\beta_1}{3} + \frac{2}{3} \sqrt{\beta_1^2 - 3\beta_2} \cos \frac{\vartheta}{3} > 0, \\ \zeta_2 &= \frac{\beta_1}{3} + \frac{2}{3} \sqrt{\beta_1^2 - 3\beta_2} \cos \left(\frac{\vartheta}{3} + \frac{2\pi}{3} \right) > 0, \quad \text{and} \\ \zeta_3 &= \frac{\beta_1}{3} + \frac{2}{3} \sqrt{\beta_1^2 - 3\beta_2} \cos \left(\frac{\vartheta}{3} + \frac{4\pi}{3} \right) > 0, \end{aligned} \tag{A23}$$

where:

$$\vartheta = \cos^{-1} \frac{2\beta_1^3 - 9\beta_1 \beta_2 + 27\beta_3}{2\sqrt{(\beta_1^2 - 3\beta_2)^3}}. \tag{A24}$$

In this case, the characteristic equation roots are:

$$\mu_1 = -\mu_2 = \sqrt{\zeta_1}, \quad \mu_3 = -\mu_4 = \sqrt{\zeta_2}, \quad \text{and} \quad \mu_5 = -\mu_6 = \sqrt{\zeta_3}. \tag{A25}$$

Appendix C. \mathcal{J} -Integral Calculation for the Crack-Tip Element

The path-independent \mathcal{J} -integral was introduced by Rice [57] as:

$$\mathcal{J} = \int_{\Gamma} \left[\omega \, dz - \left(t_x \frac{\partial u}{\partial x} + t_z \frac{\partial w}{\partial x} \right) d\Gamma \right], \tag{A26}$$

where Γ is an arbitrary integration path surrounding the crack tip, ω is the strain energy density (per unit volume), t_x and t_z are the stress vector components (referred to the outer normal to Γ), and u and w are the displacement vector components along the coordinates x and z .

For the CTE, we choose an integration path, Γ , encircling the interface between sublaminates as depicted in Figure A1. The path is subdivided into three segments, Γ_{12} , Γ_{23} , and Γ_{34} , along which quantities entering the \mathcal{J} -integral have the expressions listed in Table A1.

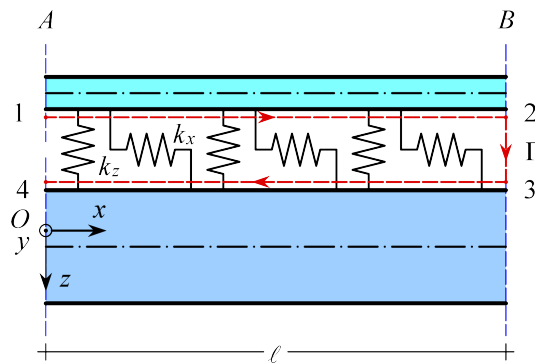


Figure A1. Integration path Γ chosen for the evaluation of the \mathcal{J} -integral for the CTE.

Table A1. Calculation of \mathcal{J} -integral.

Path Segment	dz	$d\Gamma$	ω	t_x	t_z	u	w
Γ_{12}	0	dx	-	$-\tau$	$-\sigma$	$u_1 + \varphi_1 h_1$	w_1
Γ_{23}	dz	dz	Φ/t	t_x	t_z	u	w
Γ_{34}	0	$-dx$	-	τ	σ	$u_2 - \varphi_2 h_2$	w_2

Accordingly, the following expression results:

$$\begin{aligned} \mathcal{J} = & \int_0^\ell - \left[-\tau \frac{d}{dx} (u_1 + h_1 \varphi_1) - \sigma \frac{dw_1}{dx} \right] dx + \\ & + \int_0^t \left[\frac{\Phi}{t} - \left(t_x \frac{du}{dx} + t_z \frac{dw}{dx} \right) \right] dz + \\ & + \int_\ell^0 - \left[\tau \frac{d}{dx} (u_2 - h_2 \varphi_2) + \sigma \frac{dw_2}{dx} \right] (-dx), \end{aligned} \tag{A27}$$

where t is the interface thickness and $\Phi = \Phi(\Delta w, \Delta u)$ is the interface potential energy [27], such that:

$$\sigma = \frac{\partial \Phi}{\partial \Delta w} \quad \text{and} \quad \tau = \frac{\partial \Phi}{\partial \Delta u}. \tag{A28}$$

By recalling the definition of relative displacements, Equation (6), and assuming a vanishing interface thickness ($t \rightarrow 0$), we obtain:

$$\mathcal{J} = \Phi [\Delta w(\ell), \Delta u(\ell)] - \int_0^\ell \left[\sigma(x) \frac{d\Delta w(x)}{dx} + \tau(x) \frac{d\Delta u(x)}{dx} \right] dx. \tag{A29}$$

Next, by substituting Equation (A28) into (A29) and recalling that $d\Phi$ is an exact differential, we deduce:

$$\begin{aligned}
\mathcal{J} &= \Phi [\Delta w(\ell), \Delta u(\ell)] - \int_0^\ell \left[\frac{\partial \Phi}{\partial \Delta w} \frac{d\Delta w(x)}{dx} + \frac{\partial \Phi}{\partial \Delta u} \frac{d\Delta u(x)}{dx} \right] dx = \\
&= \Phi [\Delta w(\ell), \Delta u(\ell)] - \int_{[\Delta w(0), \Delta u(0)]}^{[\Delta w(\ell), \Delta u(\ell)]} \frac{\partial \Phi}{\partial \Delta w} d\Delta w + \frac{\partial \Phi}{\partial \Delta u} d\Delta u = \\
&= \Phi [\Delta w(\ell), \Delta u(\ell)] - \int_{[\Delta w(0), \Delta u(0)]}^{[\Delta w(\ell), \Delta u(\ell)]} d\Phi.
\end{aligned} \tag{A30}$$

Hence,

$$\mathcal{J} = \Phi [\Delta w(0), \Delta u(0)], \tag{A31}$$

which holds for a general cohesive interface with potential-based traction-separation laws. For a brittle-elastic interface, the potential energy function specializes to:

$$\Phi(\Delta w, \Delta u) = \frac{1}{2}k_z\Delta w^2 + \frac{1}{2}k_x\Delta u^2. \tag{A32}$$

By substituting Equation (A32) into (A31), we obtain:

$$\mathcal{J} = \frac{1}{2}k_z\Delta w^2(0) + \frac{1}{2}k_x\Delta u^2(0), \tag{A33}$$

which is identical to Equation (42).

For the present elastic interface model, the two addends in Equation (A33) naturally identify the Mode I and II contributions to the energy release rate (see Section 4.1). This result holds for both the balanced and unbalanced cases, for which the analytical solution has been derived in Section 3. For a general cohesive interface model, Equation (A31) yields the value of the \mathcal{J} -integral, but its decomposition into Mode I and II contributions is not straightforward. The interested reader can find further hints about this issue in the papers by Wu et al. [37,38] and in the references recalled therein.

References

1. Talreja, R.; Singh, C.V. *Damage and Failure of Composite Materials*; Cambridge University Press: Cambridge, UK, 2012; ISBN 978-0-521-81942-8.
2. Garg, A.C. Delamination—A damage mode in composite structures. *Eng. Fract. Mech.* **1988**, *29*, 557–584. [CrossRef]
3. Bolotin, V.V. Delaminations in composite structures: its origin, buckling, growth and stability. *Compos. Part B Eng.* **1996**, *27*, 129–145. [CrossRef]
4. Tay, T.E. Characterization and analysis of delamination fracture in composites: An overview of developments from 1990 to 2001. *Appl. Mech. Rev.* **2003**, *56*, 1–31. [CrossRef]
5. Senthil, K.; Arockiarajan, A.; Palaninathan, R.; Santhosh, B.; Usha, K.M. Defects in composite structures: Its effects and prediction methods—A comprehensive review. *Compos. Struct.* **2013**, *106*, 139–149. [CrossRef]
6. Tabiei, A.; Zhang, W. Composite Laminate Delamination Simulation and Experiment: A Review of Recent Development. *Appl. Mech. Rev.* **2018**, *70*, 030801. [CrossRef]
7. Bucur, V. (Ed.) *Delamination in Wood, Wood Products and Wood-Based Composites*; Springer: Dordrecht, The Netherlands, 2011; ISBN 978-90-481-9549-7. [CrossRef]
8. Minatto, F.D.; Milak, P.; De Noni, A.; Hotza, D.; Montedo, O.R.K. Multilayered ceramic composites—A review. *Adv. Appl. Ceram.* **2015**, *114*, 127–138. [CrossRef]
9. Friedrich, K. (Ed.) *Application of Fracture Mechanics to Composite Materials*; Elsevier: Amsterdam, The Netherlands, 1989; ISBN 978-0-444-87286-9.
10. Carlsson, L.A.; Adams, D.F.; Pipes, R.B. *Experimental Characterization of Advanced Composite Materials*, 4th ed.; CRC Press: Boca Raton, FL, USA, 2014; ISBN 978-1-4398-4858-6.
11. Hutchinson, J.W.; Suo, Z. Mixed mode cracking in layered materials. *Adv. Appl. Mech.* **1991**, *29*, 63–191. [CrossRef]
12. Kanninen, M.F. An augmented double cantilever beam model for studying crack propagation and arrest. *Int. J. Fract.* **1973**, *9*, 83–92. [CrossRef]

13. Bruno, D.; Grimaldi, A. Delamination failure of layered composite plates loaded in compression. *Int. J. Solids Struct.* **1990**, *26*, 313–330. [[CrossRef](#)]
14. Allix, O.; Ladevèze, P. Interlaminar interface modeling for the prediction of delamination. *Compos. Struct.* **1992**, *22*, 235–242. [[CrossRef](#)]
15. Corigliano, A. Formulation, identification and use of interface models in the numerical analysis of composite delamination. *Int. J. Solids Struct.* **1993**, *30*, 2779–2811. [[CrossRef](#)]
16. Allix, O.; Ladevèze, P.; Corigliano, A. Damage analysis of interlaminar fracture specimens. *Compos. Struct.* **1995**, *31*, 61–74. [[CrossRef](#)]
17. Point, N.; Sacco, E. A delamination model for laminated composites. *Int. J. Solids Struct.* **1996**, *33*, 483–509. [[CrossRef](#)]
18. Bruno, D.; Greco, F. Mixed mode delamination in plates: a refined approach. *Int. J. Solids Struct.* **2001**, *38*, 9149–9177. [[CrossRef](#)]
19. Qiao, P.; Wang, J. Mechanics and fracture of crack tip deformable bi-material interface. *Int. J. Solids Struct.* **2004**, *41*, 7423–7444. [[CrossRef](#)]
20. Szekrényes, A. Improved analysis of unidirectional composite delamination specimens. *Mech. Mater.* **2007**, *39*, 953–974. [[CrossRef](#)]
21. Bennati, S.; Valvo, P.S. Delamination growth in composite plates under compressive fatigue loads. *Compos. Sci. Technol.* **2006**, *66*, 248–254. [[CrossRef](#)]
22. Bennati, S.; Colleluori, M.; Corigliano, D.; Valvo, P. S. An enhanced beam-theory model of the asymmetric double cantilever beam (ADCDB) test for composite laminates. *Compos. Sci. Technol.* **2009**, *69*, 1735–1745. [[CrossRef](#)]
23. Bennati, S.; Fusicaro, P.; Valvo, P.S. An enhanced beam-theory model of the mixed-mode bending (MMB) test—Part I: Literature review and mechanical model. *Meccanica* **2013**, *48*, 443–462. [[CrossRef](#)]
24. Bennati, S.; Fusicaro, P.; Valvo, P.S. An enhanced beam-theory model of the mixed-mode bending (MMB) test—Part II: Applications and results. *Meccanica* **2013**, *48*, 465–484. [[CrossRef](#)]
25. Xie, J.; Waas, A.; Rassaian, M. Analytical predictions of delamination threshold load of laminated composite plates subject to flexural loading. *Compos. Struct.* **2017**, *179*, 181–194. [[CrossRef](#)]
26. Dimitri, R.; Tornabene, F.; Zavarise, G. Analytical and numerical modeling of the mixed-mode delamination process for composite moment-loaded double cantilever beams. *Compos. Struct.* **2018**, *187*, 535–553. [[CrossRef](#)]
27. Park, K.; Paulino, G.H. Cohesive Zone Models: A Critical Review of Traction-Separation Relationships Across Fracture Surfaces. *Appl. Mech. Rev.* **2013**, *64*, 060802. [[CrossRef](#)]
28. Dimitri, R.; Trullo, M.; De Lorenzis, L.; Zavarise, G. Coupled cohesive zone models for mixed-mode fracture: A comparative study. *Eng. Fract. Mech.* **2015**, *148*, 145–179. [[CrossRef](#)]
29. Borg, R.; Nilsson, L.; Simonsson, K. Simulation of delamination in fiber composites with a discrete cohesive failure model. *Compos. Sci. Technol.* **2001**, *61*, 667–677. [[CrossRef](#)]
30. Camanho, P.P.; Dávila, C.G.; de Moura, M.F. Numerical simulation of mixed-mode progressive delamination in composite materials. *J. Compos. Mater.* **2003**, *37*, 1415–1438. [[CrossRef](#)]
31. Yang, Q.; Cox, B. Cohesive models for damage evolution in laminated composites. *Int. J. Fract.* **2005**, *133*, 107–137. [[CrossRef](#)]
32. Parmigiani, J.P.; Thouless, M.D. The effects of cohesive strength and toughness on mixed-mode delamination of beam-like geometries. *Eng. Fract. Mech.* **2007**, *74*, 2675–2699. [[CrossRef](#)]
33. Turon, A.; Dávila, C.G.; Camanho, P.P.; Costa, J. An engineering solution for mesh size effects in the simulation of delamination using cohesive zone models. *Eng. Fract. Mech.* **2007**, *74*, 1665–1682. [[CrossRef](#)]
34. Harper, P.W.; Hallett, S.R. Cohesive zone length in numerical simulations of composite delamination. *Eng. Fract. Mech.* **2008**, *75*, 4774–4792. [[CrossRef](#)]
35. Sørensen, B.F.; Jacobsen T.K. Characterizing delamination of fiber composites by mixed mode cohesive laws. *Compos. Sci. Technol.* **2009**, *69*, 445–456. [[CrossRef](#)]
36. Xie, J.; Waas, A.; Rassaian, M. Closed-form solutions for cohesive zone modeling of delamination toughness tests. *Int. J. Solids Struct.* **2016**, *88–89*, 379–400. [[CrossRef](#)]
37. Wu, C.; Gowrishankar, S.; Huang, R.; Liechti, K.M. On determining mixed-mode traction–separation relations for interfaces. *Int. J. Fract.* **2016**, *202*, 1–19. [[CrossRef](#)]

38. Wu, C.; Huang, R.; Liechti, K.M. Simultaneous extraction of tensile and shear interactions at interfaces. *J. Mech. Phys. Solids* **2019**, *125*, 225–254. [CrossRef]
39. da Silva, L.F.M.; das Neves, P.J.C.; Adams, R.D.; Speltz, J.K. Analytical models of adhesively bonded joints—Part I: Literature survey. *Int. J. Adhes. Adhes.* **2009**, *29*, 319–330. [CrossRef]
40. Bigwood, D.A.; Crocombe, A.D. Elastic analysis and engineering design formulae for bonded joints. *Int. J. Adhes. Adhes.* **1989**, *9*, 229–242. [CrossRef]
41. Krenk, S. Energy release rate of symmetric adhesive joints. *Eng. Fract. Mech.* **1992**, *43*, 549–559. [CrossRef]
42. Penado, F.E. A closed form solution for the energy release rate of the double cantilever beam specimen with an adhesive layer. *J. Compos. Mater.* **1993**, *27*, 383–407. [CrossRef]
43. Bennati, S.; Taglialegne, L.; Valvo, P.S. Modelling of interfacial fracture of layered structures. In Proceedings of the ECF 18—18th European Conference on Fracture, Dresden, Germany, 30 August–3 September 2010; ISBN 978-3-00-031802-3.
44. Liu, Z.; Huang, Y.; Yin, Z.; Bennati, S.; Valvo, P.S. A general solution for the two-dimensional stress analysis of balanced and unbalanced adhesively bonded joints. *Int. J. Adhes. Adhes.* **2014**, *54*, 112–123. [CrossRef]
45. Jiang, W.; Qiao, P. An improved four-parameter model with consideration of Poisson's effect on stress analysis of adhesive joints. *Eng. Struct.* **2015**, *88*, 203–215. [CrossRef]
46. Zhang, Z.W.; Li, Y.S.; Liu, R. An analytical model of stresses in adhesive bonded interface between steel and bamboo plywood. *Int. J. Solids Struct.* **2015**, *52*, 103–113. [CrossRef]
47. Blackman, B.R.K.; Hadavinia, H.; Kinloch, A.J.; Williams, J.G. The use of a cohesive zone model to study the fracture of fiber composites and adhesively-bonded joints. *Int. J. Fract.* **2003**, *119*, 25–46. [CrossRef]
48. Li, S.; Thouless, M.D.; Waas, A.M.; Schroeder, J.A.; Zavattieri, P.D. Mixed-mode cohesive-zone models for fracture of an adhesively bonded polymer–Matrix composite. *Eng. Fract. Mech.* **2006**, *73*, 64–78. [CrossRef]
49. Jones, R.M. *Mechanics of Composite Materials*, 2nd ed.; Taylor & Francis Inc.: Philadelphia, PA, USA, 1999; ISBN 978-1560327127.
50. Schapery, R.A.; Davidson, B.D. Prediction of energy release rate for mixed-mode delamination using classical plate theory. *Appl. Mech. Rev.* **1990**, *43*, S281–S287. [CrossRef]
51. Valvo, P.S. On the calculation of energy release rate and mode mixity in delaminated laminated beams. *Eng. Fract. Mech.* **2016**, *165*, 114–139. [CrossRef]
52. Tsokanas, P.; Loutas, T. Hygrothermal effect on the strain energy release rates and mode mixity of asymmetric delaminations in generally layered beams. *Eng. Fract. Mech.* **2019**, *214*, 390–409. [CrossRef]
53. Taglialegne, L. Modellazione Meccanica Della Frattura Interlaminare di Provini in Composito Non Simmetrici. Master's Thesis, University of Pisa, Pisa, Italy, 2014. Available online: <http://etd.adm.unipi.it/theses/available/etd-09172014-092832> (accessed on 23 July 2019).
54. Davidson, B.D.; Hu, H.; Schapery, R.A. An Analytical Crack-Tip Element for Layered Elastic Structures. *J. Appl. Mech.* **1995**, *62*, 294–305. [CrossRef]
55. Wang, J.; Qiao, P. Interface crack between two shear deformable elastic layers. *J. Mech. Phys. Solids* **2004**, *52*, 891–905. [CrossRef]
56. Timoshenko, S.P. *Strength of Materials, Vol. 1: Elementary Theory And Problems*, 3rd ed.; D. Van Nostrand: New York, NY, USA, 1955; ISBN 978-0442085414.
57. Rice, J.R. A path independent integral and the approximate analysis of strain concentrations by notches and cracks. *J. Appl. Mech.* **1968**, *35*, 379–386. [CrossRef]
58. Arouche, M.M.; Wang, W.; Teixeira de Freitas, S.; de Barros, S. Strain-based methodology for mixed-Mode I+II fracture: A new partitioning method for bi-material adhesively bonded joints. *J. Adhes.* **2019**, *95*, 385–404. [CrossRef]
59. Vannucci, P.; Verchery, G. A special class of uncoupled and quasi-homogeneous laminates. *Compos. Sci. Technol.* **2001**, *61*, 1465–1473. [CrossRef]
60. Garulli, T.; Catapano, A.; Fanteria, D.; Jumel, J.; Martin, E. Design and finite element assessment of fully uncoupled multi-directional layouts for delamination tests. *J. Compos. Mater.* **2019**. [CrossRef]
61. Samborski, S. Numerical analysis of the DCB test configuration applicability to mechanically coupled Fiber Reinforced Laminated Composite beams. *Compos. Struct.* **2016**, *152*, 477–487. [CrossRef]
62. Bennati, S.; Valvo, P.S. An experimental compliance calibration strategy for mixed-mode bending tests. *Proc. Mater. Sci.* **2014**, *3*, 1988–1993. [CrossRef]

63. Sørensen, B.F.; Jørgensen, K.; Jacobsen, T.K.; Østergaard, R.C. DCB-specimen loaded with uneven bending moments. *Int. J. Fract.* **2006**, *141*, 163–176. [[CrossRef](#)]
64. Davidson, B.D.; Gharibian, S.J.; Yu, L. Evaluation of energy release rate-based approaches for predicting delamination growth in laminated composites. *Int. J. Fract.* **2000**, *105*, 343–365. [[CrossRef](#)]
65. Davidson, B.D.; Bialaszewski, R.D.; Sainath, S.S. A non-classical, energy release rate based approach for predicting delamination growth in graphite reinforced laminated polymeric composites. *Compos. Sci. Technol.* **2006**, *66*, 1479–1496. [[CrossRef](#)]
66. Harvey, C.M.; Wang, S. Experimental assessment of mixed-mode partition theories. *Compos. Struct.* **2012**, *94*, 2057–2067. [[CrossRef](#)]
67. Harvey, C.M.; Eplett, M.R.; Wang, S. Experimental assessment of mixed-mode partition theories for generally laminated composite beams. *Compos. Struct.* **2015**, *124*, 10–18. [[CrossRef](#)]
68. Bednarczyk, B.A.; Aboudi, J.; Yarrington, P.W.; Collier, C.S. Simplified Shear Solution for Determination of the Shear Stress Distribution in a Composite Panel From the Applied Shear Resultant. In Proceedings of the 49th AIAA/ASME/ASCE/AHS/ASC Structures, Structural Dynamics, and Materials Conference, Schaumburg, IL, USA, 7–10 April 2008. [[CrossRef](#)]
69. Kumar, R.; Nath, J.K.; Pradhan, M.K.; Kumar, R. Analysis of Laminated Composite Using Matlab. In Proceedings of the ICMEET 2014—1st International Conference on Mechanical Engineering: Emerging Trends for Sustainability, MANIT, Bhopal, India, 29–31 January 2014.
70. Wallner-Novak, M.; Augustin, M.; Koppelhuber, J.; Pock, K. *Cross-Laminated Timber Structural Design*; proHolz: Vienna, Austria, 2018; Volume II, ISBN 978-3-902320-96-4.



© 2019 by the authors. Licensee MDPI, Basel, Switzerland. This article is an open access article distributed under the terms and conditions of the Creative Commons Attribution (CC BY) license (<http://creativecommons.org/licenses/by/4.0/>).